The photochemistry of irradiated Enceladus ice analogues
Implications for the formation of ozone and carbon trioxide

Bründl, T. M.; Terwisscha van Scheltinga, J.; Cazaux, S.; Chuang, K. J.; Linnartz, H.

DOI
10.1016/j.icarus.2025.116751

Publication date
2026

Document Version
Final published version

Published in
Icarus

Icarus 444 (2026) 116751

Contents lists available at ScienceDirect

Icarus

journal homepage: www.elsevier.com/locate/icarus

Research Paper

The photochemistry of irradiated Enceladus ice analogues: Implications for the formation of ozone and carbon trioxide

T.-M. Bründl [a,b,*], J. Terwisscha van Scheltinga [b], S. Cazaux [a,b], K.-J. Chuang [b], H. Linnartz [b]

[a] Department of Space Engineering, Delft University of Technology, 2629 HS Delft, The Netherlands
[b] Laboratory for Astrophysics, Leiden Observatory, Leiden University, P.O. Box 9513, NL-2300 RA Leiden, The Netherlands

ARTICLE INFO

Keywords:
Astrobiology
Astrochemistry
Enceladus
Experimental techniques
Ices, IR spectroscopy
Photochemistry
Satellites, Composition
Satellites, Surfaces
Saturn, Satellites
Solar radiation

ABSTRACT

Detailed observations of Enceladus by the Cassini spacecraft revealed its astrobiological potential and transformed our perception of ocean worlds in the Solar System. Beneath Enceladus' icy crust lies a warm ocean sustained by tidal heating. This ocean expels subsurface material through fissures at the south pole region into space as plumes. The particles in these plumes reaccrete on Enceladus' surface, while some of the volatiles present in the sub-surface ocean diffuse through the ice shell to reach the surface. In this study, we irradiated thin Enceladus ice analogues in an ultra-high vacuum chamber optimised for ice chemistry at a surface temperature of 70 ± 2 K and compared the resulting composition with ices typical to the ISM (15 K). We studied the irradiation of ices composed of H_2O, CO_2, and NH_3 mixtures as a function of wavelength by using two different radiation sources that cover high and low photon energy ranges: The microwave-discharge hydrogen-flow lamp (MDHL) generating vacuum-ultraviolet (VUV) light, that is, between 115 - 180 nm, and the solar radiation Xe-arc lamp (SRL), simulating the solar broadband radiation from 200 nm - 1800 nm. Upon irradiation, solid-state photoproducts were identified using a Fourier-transform infrared (FTIR) spectrometer in the mid-infrared range (4000 - 700 cm^{-1} or 2.5 - 14.3 μm). Sublimating gas-phase species were tracked using a quadrupole mass spectrometer (QMS). At 70 K, energetic photons from the MDHL formed new species such as O_3 and CO_3 in an H_2O:CO_2:NH_3 ice matrix due to the clustering of CO_2 at elevated temperatures. Hereby, dissociation of segregated CO_2 provides the necessary oxygen atoms to form O_3 via the enhanced mobility and addition reaction of O-atoms. At 15 K, CO, OCN^-, H_2CO, CH_3OH, HCOOH and possibly NH_2OH were induced by VUV-photons. Similarly, these species were detected at 70 K with a tentative assignment for HCOOH and NH_2OH. The SRL caused no chemical evolution of the ice due to insufficient photon energies. In conclusion, we predict the formation of ozone by gardening of CO_2-rich or mixed CO_2:H_2O ice, found, for example, in-between the tiger stripes on Enceladus or on other icy bodies in our Solar System with surface temperatures cooler than 88 K.

1. Introduction

In the last decades numerous ocean-bearing moons, or "ocean worlds", have been discovered in our Solar System. To date, Enceladus is the best studied ocean world, owing to the wealth of observational data provided by the instrument suite on-board the Cassini spacecraft (Schenk et al., 2018). Re-analysis of Cassini data showed that the ocean of Enceladus is the only known ocean besides that of Earth containing phosphorus, hereby completing the list of bio-critical elements (CHNOPS) and fulfilling the requirements for habitability as we know it (Postberg et al., 2023).

With the Cosmic Dust Analyser (CDA) Cassini measured the plumes' material in-situ during close moon flybys, linking its origin to a global ocean of appreciable size (Hsu et al., 2015). Cassini's magnetometer revealed a diffuse atmosphere driven by water plumes that emanate from the South Polar Terrain (SPT) on Enceladus (Dougherty et al., 2006). This region is characterised by four distinct fractures, labelled tiger stripes, from which plumes expel a mixture of icy grains and

* Corresponding author at: Department of Space Engineering, Delft University of Technology, 2629 HS Delft, The Netherlands.
E-mail address: t.brundl@tudelft.nl (T.-M. Bründl).

https://doi.org/10.1016/j.icarus.2025.116751
Received 19 February 2025; Received in revised form 17 July 2025; Accepted 19 July 2025
Available online 28 August 2025

vapour (Porco et al., 2006) with an estimated solid ice fraction between 0.07–0.2 (Kieffer et al., 2009; Gao et al., 2016).

Cassini INMS measurements of the E14, E17, E18, and E21 flybys revealed the plumes vapour mixing ratio by means of the major fragmented mass of a molecule (Waite et al., 2017): H_2O (96%–99%), CO_2 (0.3–0.8%), CH_4 (0.1–0.3%), NH_3 (0.4–1.3%), and H_2 (0.4–1.4%). In addition, Postberg et al. (2018) found traces of macromolecular organic species using CDA data. The Visual and Infrared Mapping Spectrometer (VIMS) mapped the surface of Enceladus and detected simple and unassigned organics at the SPT (Brown et al., 2006), while none were found elsewhere on the moon with VIMS or ground-based telescopes (Cruikshank et al., 2005; Emery et al., 2005).

In contrast, pure CO_2 was observed in higher concentrations at the SPT (Combe et al., 2019). Matson et al. (2018) hypothesised an endogenic mechanism behind this finding in which CO_2 exsolves in the form of bubbles at the oceanic table and accumulates within gas pockets embedded in the ice sheet. These gas pockets can rupture, allowing the CO_2 gas to escape through small fissures and cracks appearing in the icy crust due to flexing from tidal forces. The gas gradually cools while seeping to the surface and freezes in deposits, given sufficiently cold surface temperatures (Matson et al., 2018).

The different molecules on the surface of Enceladus are relentlessly exposed to radiation such as charged particles from Saturn's magnetosphere, solar wind, galactic cosmic rays, and UV photons (Sect. 11.2.2 in Dougherty et al. (2009)). These types of radiation trigger various physico-chemical processes of the ice. Molecular ice can be dissociated upon irradiation with UV photons or energetic particles (Cassidy et al., 2010; Öberg, 2016; Cuppen et al., 2017). Radicals, free atoms, and molecules can form new species when they meet with each other (Linnartz et al., 2015; Cuppen et al., 2024). Several experimental studies have shown that complex organic species can form in the solid phase either by photodissociation and subsequent reactions of photofragments (Muñoz Caro et al., 2002; Bernstein et al., 2002; Öberg et al., 2009a), by ion irradiation (Modica and Palumbo, 2010), electron bombardment (Maity et al., 2015), or via atom and radical addition reactions at low temperatures (Fedoseev, 2014; Linnartz et al., 2015). For photon irradiation, fragments resulting from the photodissociated parent species may diffuse across the ice surface and recombine to form new photoproducts. With regards to the composition of Enceladean ices, the photon- and ion-induced ice chemistry of water, ammonia, and carbon dioxide ice mixtures have been studied extensively at cold temperatures (below 20 K) in the laboratory (Chen et al., 2011; Lv et al., 2014; Potapov et al., 2022).

Several research groups have conducted laboratory investigations of ices at warmer temperatures relevant to those of ocean world surfaces (Mastrapa et al., 2008; Hudson and Gerakines, 2023; Bramble and Hand, 2024; Chandra et al., 2025), whereby irradiation experiments have mainly focussed on the radiolysis of planetary ices. Nölle et al. (2024) proposes that degradation of the organic component found in Type 2 (organic-rich) icy grains is driven predominantly by radiation from photons rather than plasma sputtering on their radially outward journey from Enceladus to the E-ring. To that end, we selected solar photons as a radiation source to study the temperature-dependent photolysis of ices at temperatures near those found on average at Enceladus of 70 K (Spencer et al., 2006). In short, the aim of this research is to study the effect of photons from different solar radiation sources (Vacuum-Ultraviolet/UV–Vis) on the processing of Enceladus ice analogues and to investigate the chemical complexity induced by such processes.

This paper investigates the photon-induced chemistry of the surface ice (H_2O:CO_2:NH_3) at Enceladus-representative temperatures of 70 K. Specifically, we analysed the chemical complexity upon irradiation with different radiation sources. In this paper, we first describe the experimental setup and data analysis (Section 2). Section 3 presents our experimental results, while Section 4 on the discussion applies our findings to Enceladus and other icy moons in our Solar System. Section 5 provides a summary and conclusion of our research. Finally, the Appendices A–D comprise supporting material such as results from control experiments.

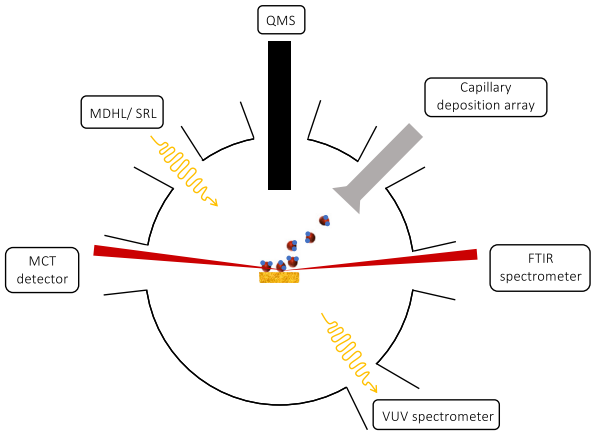

Fig. 1. Simplified CryoPAD2 setup showing a top view of the chamber's outline and the cryogenically cooled substrate in its centre. Attached to the chamber are the QMS, FTIR, interchangeable radiation source, that is, MDHL or SRL, as well as the capillary deposition array through which the molecules enter the chamber for deposition.

2. Experimental setup and data analysis

2.1. CryoPAD2

Analogues of Enceladus-like ices were grown and irradiated using the Cryogenic Photoproduct Analysis Device 2 (CryoPAD2) housed within the Laboratory of Astrophysics at Leiden Observatory in the Netherlands. In brief, the setup operates at ultra-high vacuum (UHV) conditions with a base pressure below 10^{-10} mbar and facilitates cryogenic cooling and heating of a gold-plated copper cold-finger between 14–300 K with a relative and absolute accuracy of ±1 K and ±2 K, respectively. In essence, a two-stage closed-cycle helium-cryostat cools a cold-finger to 14 K, while a heating foil provides a counteracting heat input through an auto-tuned PID cycle, managed by a LakeShore 350 controller and enabling a temperature stability of the substrate within 0.2 K. Fig. 1 illustrates besides other components a high precision leak valve attached to a capillary deposition array. This creates a directional beam of gas-phase molecules to flow to and adsorb on a 1 cm^2 large substrate, located at the bottom of the copper cold-finger within a ∼4 cm distance from the deposition array.

A microwave-discharge hydrogen-flow lamp (MDHL), operating at an H_2 flow pressure of 0.4 ± 0.01 mbar, irradiates the deposited ice analogues through a MgF_2 window at a distance of 31 cm from and a 45° angle to the substrate. This allows for simultaneous observations of the studied ice in the infrared regime. The VUV light emitted by the MDHL is composed mostly of Lyman-α at 121.6 nm, as well as H_2 emission lines between 140–170 nm as shown in Fig. 2(a). This spectrum is acquired in-situ by a VUV spectrometer. Specifically, a McPherson Model 234 is mounted on the opposite side of the MDHL.

The wavelength-specific photon flux, $\phi(\lambda)$, is determined from Eq. (1), where the total VUV current is measured by a NIST calibrated SXUV-100 photodiode (EQ Photonics). The quantum efficiency, η, attributed to each wavelength, $\eta(\lambda)$ is provided by the same supplier. By integrating Eq. (1) and using the known electron charge, C, a VUV photon flux of $(2.26 \pm 0.02) \times 10^{14}$ photons cm^{-2} s^{-1} and energy flux of $(2.09 \pm 0.02) \times 10^{15}$ eV cm^{-2} s^{-1} is calculated. Further specifics of CryoPAD2 are available in the literature (i.e., most recently in chapter 2.2 of Terwisscha van Scheltinga (2021) and Ligterink et al. (2018)).

$$\phi(\lambda) = \frac{i(\lambda)}{\eta(\lambda) \times C} \tag{1}$$

In this study, the MDHL is replaced with another radiation source for certain experiments. In specific, a Xe-arc lamp (MKS Instruments),

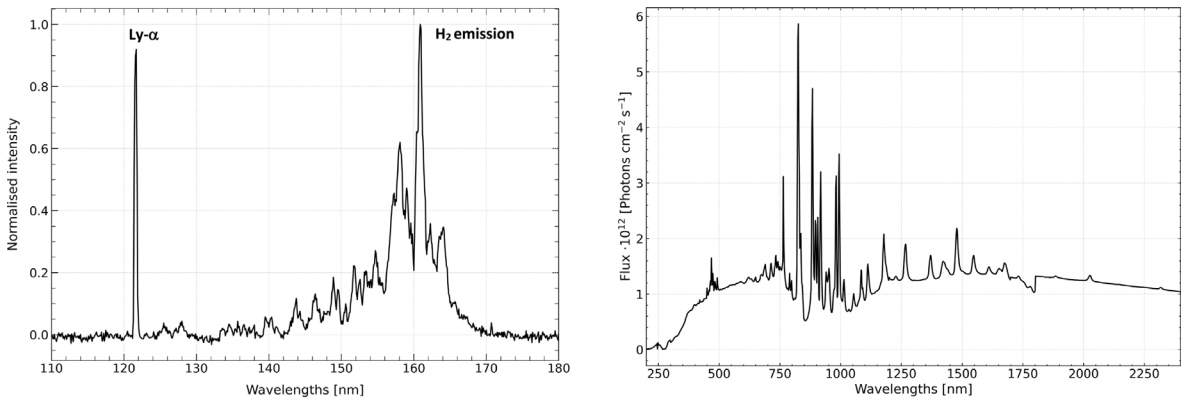

(a) (b)

Fig. 2. (a) VUV spectrum of the MDHL lamp recorded between 110 and 180 nm with the Lyman-α at 121.6 nm and the H_2 emission lines between 140 and 170 nm. The VUV spectrum is normalised to the H_2 emission peak at ~160 nm. (b) Xe-arc spectrum (solar radiation lamp) showing strong xenon emission lines (800–1100 nm) which have been reduced with a customised airmass filter AM0 for outer space (MKS Instruments).

Table 1
A summary of radiation sources in the laboratory and at Enceladus with their respective photon and energy fluxes as well as the energy flux ratios.

Radiation source	Photon flux (photons cm^{-2} s^{-1})		Energy flux (eV cm^{-2} s^{-1})		Energy flux ratio
	Enceladus[a]	Laboratory	Enceladus[a]	Laboratory	(Lab./Enceladus)
Lyman-α UV-C/H_2 emissions	3.3×10^9 1.1×10^{12}	2.3×10^{14}	3.3×10^{10} 4.7×10^{13}	2.1×10^{15}	~44[b]
SRL	2.2×10^{15}[c]	2×10^{15}	4.4×10^{15}	2.6×10^{16}	~0.17
Magnetospheric plasma	1.1×10^{10}[d]	–	3.3×10^{10}[d]	–	~1400[e]

Note. — [a]Flux values taken from Madey et al. (2002) at Earth and scaled to the Sun-Enceladus distance (9.5 AU). [b]The energy flux at Enceladus is composed of Ly-α and H_2 emission/UV-C contributions. [c]The solar radiation photons are assumed to mainly originate from the IR range. [d]This value is taken from Madey et al. (2002) for Dione, assuming Enceladus receives a comparable flux for the magnetospheric plasma. [e]The ratio corresponds to the energy flux value for the incident UV at Enceladus/magnetospheric plasma.

hereafter referred to as solar radiation lamp (SRL), has a different spectral energy distribution (SED) compared to the MDHL and emits the majority of its light at longer wavelengths between 200–1800 nm (Fig. 2(b)) with a photon flux of $\sim 2 \times 10^{15}$ photons cm^{-2} s^{-1} and energy flux of $\sim 2.6 \times 10^{16}$ eV cm^{-2} s^{-1}. Further, an airmass filter is placed between the lamp and the MgF_2 window to considerably reduce the intensity of unfavourable xenon emission lines from the Xe-arc lamp, providing a closer spectral match to the Sun's extraterrestrial solar spectrum. The flux scaling between the VUV/SRL and at Enceladus is essential to extrapolate laboratory processes to geologically relevant timescales and is shown in Table 1.

In order to deduce the chemical reactions occurring in the ice during photon irradiation CryoPAD2 offers two diagnostic tools. A Fourier-transform infrared (FTIR) spectrometer (Agilent 660) collects infrared spectra by means of Reflective Absorption Infrared spectroscopy (RAIRS) as illustrated in Table 2, whereby a focused infrared beam enters the vacuum chamber at a grazing angle, is reflected by the substrate, and redirected into a mercury-cadmium-telluride (MCT) detector. The infrared optical path outside the vacuum chamber is purged with dry air, that is, air where both H_2O and CO_2 are removed, to prevent absorption of infrared light by these species. The FTIR-captured infrared spectra allow for the identification and quantification of solid-state species during photon irradiation at sub-monolayer sensitivity.

Simultaneously, in our experiments gas-phase species desorbing from the surface of the ice are identified qualitatively by a quadrupole mass spectrometer (Hiden HAL series 1000 PIC), in short QMS. The electrons emitted from the filament ionises the species in the chamber at ~70 eV and causes the intact species to fragment into its constituents, giving a distinct fragmentation pattern. Not only are newly formed species detected during the irradiation process at constant temperatures, but furthermore the temperature programmed desorption (TPD) method can reveal trapped molecules and atoms. Hereby, the substrate is heated with a ramping rate of 5 K min^{-1}, causing a release of species from the ice at their characteristic desorption temperatures. During the TPD, the rise of mass signals can be associated with the disappearance of an IR features at the corresponding temperatures. By subtracting the spectrum before irradiation from the spectrum after irradiation, positive and negative absorbance values indicate the formation and destruction of molecular species, or change of IR bands due to ice restructuring. These difference spectra are complementary to the TPD measurements as they reveal subtle changes in the IR spectrum.

2.2. Experimental procedure

To prepare the pure and multi-ice mixtures the following gases are used and listed with their provider and purity: H_2O (Sigma-Aldrich Milli-Q®, 97%), CO_2 (Linde, 99.999%), NH_3 (Praxair, 99.96%). H_2 (Linde, 99.999%) is required to operate the MDHL.

The gas mixtures are prepared in the mixing line with a base pressure below 10^{-4} mbar. The mixing line connects to an all-metal leak valve that controls the flow of gas-phase molecules into the main chamber through a capillary array consisting of a multitude of glass capillaries. Hence, a directional beam of gas can be deposited at a 45° angle to the surface normal and an average deposition pressure of $\sim 10^{-9}$ mbar in the main chamber. The movable capillary array is positioned 40 mm from the substrate which allows for continuous infrared measurements in order to precisely control the ice thickness in real time. The thin ice film is deposited and irradiated at the same temperature.

A list of performed experiments containing their operational parameters is shown in Table 2. All tertiary ices (H_2O:CO_2:NH_3) measured a 2:1:1 ratio in the solid state following the preparation of the gas-phase

Table 2
An overview of all performed experiments and their operational properties on the CryoPAD2 setup.

Radiation source	Species	Temperature(K)	Mixing ratios in the gas-phase	Ice thickness (monolayers)
MDHL	H_2O	15	1	25
	H_2O	70	1	40
	CO_2	15	1	31
	CO_2[a]	70	1	31
	NH_3	15	1	32
	NH_3	70	1	32
	$H_2O:CO_2$[a]	70	9:1	56
	$H_2O:NH_3$[a]	70	9:1	115
	$H_2O:CO_2:NH_3$	15	50:4:1	51
	$H_2O:CO_2:NH_3$	70	28:3:1	75
SRL	$H_2O:CO_2:NH_3$	70	52:6:1	83

Note. — [a]Control experiment.

mixture in the mixing line at empirically determined partial pressures. The ice mixing ratios are determined in situ by converting the IR absorption area into absolute column density (molecules per area; Eq. (2)) with IR absorption strength values available in the literature (Table 3), where 1 monolayer is defined as 10^{15} molecules per cm^2.

2.3. Data analysis for photoproduct identification

During VUV irradiation, dipole-active photoproducts can be identified in the ice matrix by tracing their characteristic spectral bands in the mid-infrared range. As the photoproducts are located mainly in the bulk of the ice, albeit sparsely, the molecule's signature from photodesorption is too low to be detected in the QMS and will not be used further for the data analysis. Instead, the QMS is used primarily to trace species during the TPD phase at the end of the experiment, where species are released at their characteristic desorption temperature when the substrate is heated. The infrared spectra are used to correlate the disappearance of infrared absorption bands with the species detected with the QMS at given time, and confirming the detection of a photoproduct. These two complementary tools secure the identification of overlapping mass fragments of different species or convoluted IR spectral bands of photoproducts and parent species. The following sections describe concretely the data analysis of vibrational spectroscopy and mass spectrometry for photoproduct identification.

2.3.1. Vibrational spectroscopy by means of RAIRS

All mid-infrared spectra are baseline subtracted, whereby a baseline is fit to segments devoid of spectral bands and subtracted from the entire spectrum. The known spectral positions and associated transmission band strengths shown in Table 3 are used to assign and quantify (the parent) chemical species at lower and higher temperatures in Section 3. The band strengths of pure ices are used to determine the ratio of parent species in the ice mixture.

The FTIR in RAIRS configuration collects mid-infrared spectra from 4000 to 700 cm^{-1} (2.5–14.3 μm) with a 1 cm^{-1} resolution. This is followed by data processing whereby the column density, $N_{species}$, for the species in question is determined from the following equation:

$$N_{species} = \ln(10) \times \frac{\int_{band} \mathrm{Abs}\, d\nu}{A' \times R} \quad (2)$$

where $\int_{band} \mathrm{Abs}\, d\nu$ is the integrated absorbance band area and A′ is the apparent band strength for transmission infrared spectroscopy in cm $molecule^{-1}$ taken from the literature (listed in the last column of Table 3). For the current RAIRS setting, a correction factor, R, must be applied to account for the conversion from transmission to reflection spectroscopy. This setup-dependent value is experimentally derived from isothermal desorption of CO and has previously been determined for CryoPAD2 to be 4.5 (Ligterink et al., 2018; Terwisscha van Scheltinga et al., 2022).

2.3.2. Mass spectrometry

Every QMS device measures different mass-to-charge (m/z) signals due to its intrinsic mass sensitivity. Therefore, the measured m/z values have to be corrected accordingly. By measuring the abundance of noble gases from a known gas mixture the mass sensitivity function can be determined. Table 4 shows the characteristic peak desorption temperatures for relevant parent species and photoproducts with their primary and secondary mass fragments, if available.

3. Results

This section comprises the findings from the experiments presented in Table 2, whereby two main themes are covered. First, the effect of temperature (15 K vs. 70 K) on the parent species is explored for pure ices and a tertiary ice mixture as an analogue of ices on the surface of Enceladus. Secondly, we present the effect of VUV vs. solar fluence on ice mixtures of the same ratio.

3.1. Temperature effect on ice IR features

3.1.1. Pure ices: H_2O, CO_2 and NH_3

Ice deposition at different temperatures results in distinct solid-state structures, that is amorphous, compact, or crystalline forms, as observed by their IR vibrational transitions. The characterisation of IR features resulting from pure ices, including H_2O, CO_2, and NH_3, is shown in Fig. 4 and summarised in Table 5.

For H_2O in Fig. 4, the modes for the dominant stretching (ν_1), weak bending (ν_2) and moderate libration (ν_R) of the molecules can be seen from left to right. At 15 K compared to 70 K, the ν_1 band redshifts by ~10 cm^{-1} from 3411 to 3400 cm^{-1} with a shoulder appearing at ~3300 cm^{-1}, while the ν_R spectral position blueshifts by ~20 cm^{-1} from 861 to 883 cm^{-1}. While both ν_1 and ν_R appear sharper, ν_2 (middle) becomes smoother and does not change its position significantly. Furthermore, the disappearance of the weak OH dangling mode at 70 K (~3697 cm^{-1} seen at 15 K) may be owed to ice compaction or smaller pores coalescing into larger pores during heating and the subsequent decrease of surface area inferring a reduction in OH molecules protruding from the surface (Cazaux et al., 2015). The shift in spectral positions, sharpening of the ν_1 and ν_R mode, and the disappearance of the OH-dangling mode hint at a global restructuring of the ice at 70 K compared to 15 K. In relation to literature values, the bending modes are in good agreement with Gerakines et al. (1995) and Mastrapa et al. (2009), whereas the stretching and libration modes differ significantly from the values given in Table 3. Baratta and Palumbo (1998) suggest that differences in spectral features can arise between transmission spectroscopy and RAIRS. A full comparison of absorption bands to literature values is missing at 70 K due to a general lack of information at this temperature.

In the case of CO_2, the strongest band in the mid-IR range is the asymmetric stretching mode (ν_3) which is split into three peaks. Hereby, the interplay of phonon vibrations with the E-field of the UV-radiation results in two modes at 2387 cm^{-1} (LO) and 2342 cm^{-1} (TO), collectively termed as LO-TO splitting. This coupling effect occurs at a grazing angle of the incident UV-light and manifests itself in unique IR band profiles for polarisation sensitive species, explained in more detail by Baratta and Palumbo (1998) and Baratta et al. (2000). Evidently, laboratory experiments employing a normal incidence angle do not observe the LO mode near 2387 cm^{-1} for CO_2 (Gerakines et al., 1995; Ehrenfreund et al., 1997; van Broekhuizen et al., 2006). Further, this band characterises CO_2 clusters (Edridge et al., 2013) and can be seen both at 15 and 70 K due to a sufficiently high surface coverage required to form these clusters, proposed by He et al. (2017). In this

Table 3
Characteristic spectral bands and band strengths of solid-state parent species and photoproducts in various ice matrices at low and high temperatures.

Species	Peak position (cm^{-1})	Ice Matrix	Temp. (K)	A′ (cm^{-1})	Reference
Parent species					
CO_2	3708	CO_2	14	2.1×10^{-18}	Gerakines et al. (1995)
	3708	CO_2	25	1.8×10^{-18}	Bouilloud et al. (2015)
NH_3	1071	NH_3	18	2.0×10^{-17}	Hudson et al. (2022)
	1057	NH_3	100	2.2×10^{-17}	Hudson et al. (2022)
	3370	NH_3	18	2.6×10^{-17}	Hudson et al. (2022)
	3376	NH_3	100	3.1×10^{-17}	Hudson et al. (2022)
H_2O	760	H_2O	14	3.3×10^{-17}	Gerakines et al. (1995)
	763	H_2O	25	3.2×10^{-17}	Mastrapa et al. (2009)
	3280	H_2O	14	2.2×10^{-16}	Gerakines et al. (1995)
	3297	H_2O	25	1.5×10^{-16}	Bouilloud et al. (2015)
Photoproducts					
$^{13}CO_2$	2283	CO_2	14	–	Gerakines et al. (1995)
$^{13}CO_2$	2283	CO_2	25	–	Bouilloud et al. (2015)
CO	2139	CO	14	–	Gerakines et al. (1995)
	2139	CO	25	–	Bouilloud et al. (2015)
CO_3	1879	CO_2	10	–	Bennett et al. (2004)
	2044	CO_2	10	-	Bennett et al. (2004)
H_2CO	1496	H_2O:H_2CO	10	–	Schutte et al. (1993)
	1500	H_2CO	25	–	Bouilloud et al. (2015)
	1719	H_2O:H_2CO	10	–	Schutte et al. (1993)
	1725	H_2CO	25	–	Bouilloud et al. (2015)
HCOOH	1229	HCOOH:H_2O:$C^{18}O_2$	15	–	Bisschop et al. (2007)
	1224	HCOOH:H_2O	75	–	Bisschop et al. (2007)
	1383	HCOOH:H_2O	10	–	Schutte et al. (1999)
	1383	HCOOH:H_2O	80	–	Schutte et al. (1999)
	1695	HCOOH:H_2O:$C^{18}O_2$	15	–	Bisschop et al. (2007)
	1709	HCOOH:H_2O	75	–	Bisschop et al. (2007)
O_3	1045	CO_2	20	–	Brewer and Wang (1972)
OCN^-	2166	H_2O:HNCO:NH_3	120	–	van Broekhuizen et al. (2005)

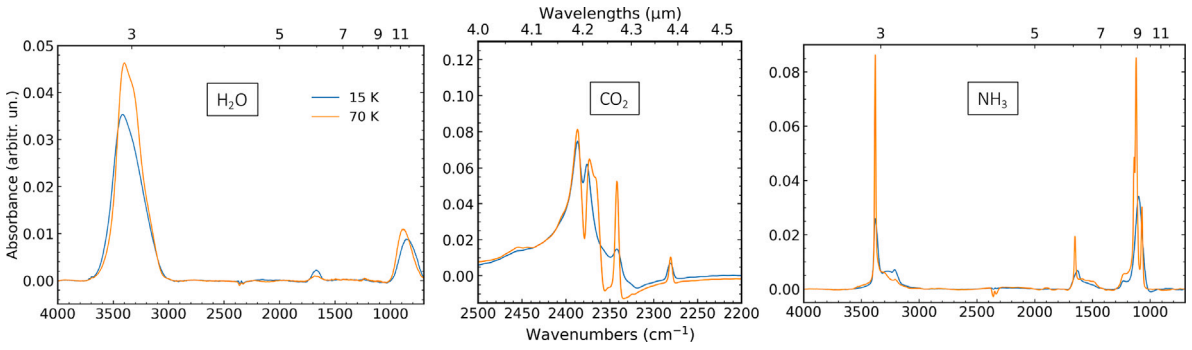

Fig. 3. (a) IR spectra of H_2O:CO_2:NH_3 (2:1:1 ratio) ice at 15 K (blue) and 70 K (orange). (b) In the magnified region between 3500–3800 cm^{-1}, covering both CO_2 combination modes, the O-H dangling bond at ~3655 cm^{-1} is only visible at 15 K. An offset has been introduced between the spectra for clarity.

work, the peak at 2342 cm^{-1} is assigned to physisorbed CO_2 onto the water surface with its position remaining unchanged independent of the temperature. However, the full width at half maximum (FWHM) of the absorption band decreases at 70 K, resulting in a sharper IR feature. The third peak redshifts by 3 cm^{-1} from 2376 cm^{-1} to 2373 cm^{-1} at 15 K and forms a shoulder near 2366 cm^{-1} at 70 K. While this peak is widely unknown in the literature, Edridge et al. (2013) assigns it to the weakly polarised LO phonon mode based on the change of the phonon vibrations in the ice. The authors report a similar shift during a temperature increase of the ice from 28 to 55 K. The two combination modes at ~3597 and 3705 cm^{-1} do not change significantly with temperature and are thus only presented in Table 3. Additionally, the isotopologue $^{13}CO_2$ is observed at 2281 cm^{-1} for higher and lower temperatures without notable band shifts or shape changes.

The change of NH_3 mid-IR features with temperature is more prominent: The peaks for the stronger N–H asymmetric stretching mode (ν_3) at ~3380 cm^{-1} and weaker symmetric stretching mode (ν_1) at ~3210 cm^{-1} become more distinct at higher temperatures, with the smaller peak decreasing in absorbance and slightly shifting from 3212 to 3207 cm^{-1}. The plateau separating the peaks disappears and transforms into a slope. This profile change agrees with the experimental results for solid NH_3 by Hudson et al. (2022). The N–H bending mode (ν_4) at ~1630 cm^{-1} becomes narrower with the peak shifting by ~20 cm^{-1} to higher wavenumbers, while the umbrella mode (ν_2) at ~1101 cm^{-1} splits into 3 peaks: The smallest at ~1440 cm^{-1}, the highest near 1123 cm^{-1}, and intermediate at ~1072 cm^{-1}, which indicates the transition from an amorphous to a crystalline ice structure (Giuliano et al., 2014). The ν_1/ν_3 and ν_4 band positions are in good agreement with literature (see Table 3). For ν_2, Hudson et al. (2022) report values differing by ~30 and 15 cm^{-1} for low (18 K) and high temperatures (100 K), respectively. Thus, our experiments infer that the position and profile shape of absorption bands may inform the thermal history of the ice. With increasing temperature, we observe a change in porosity and increase of crystallisation in the absence of irradiation.

3.1.2. *Tertiary ices: H_2O:CO_2:NH_3 (2:1:1)*

IR spectra obtained from the H_2O:CO_2:NH_3 (2:1:1) ice mixtures at 70 K and 15 K are shown in Fig. 3. Several IR features overlap,

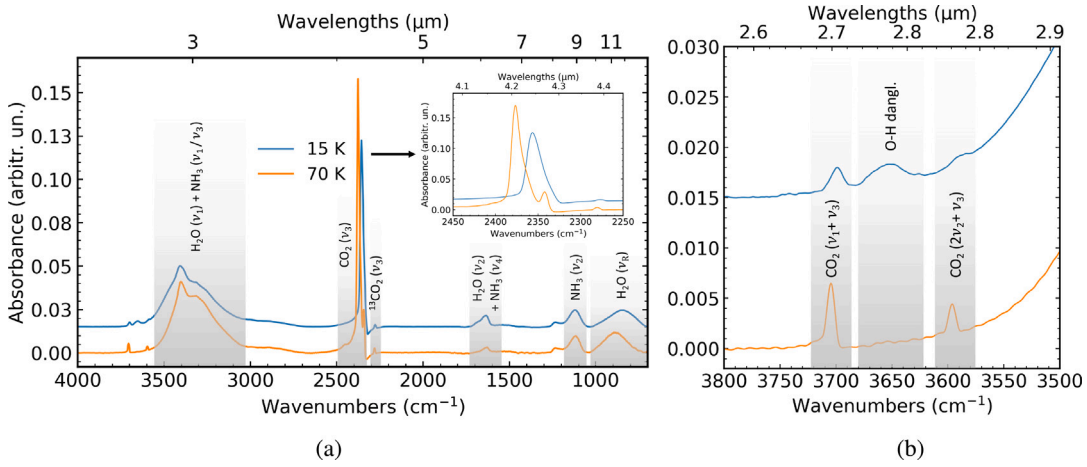

Fig. 4. IR spectra of pure ices (from left to right: H_2O, CO_2, NH_3) were measured at 15 (blue) and 70 K (orange). In the H_2O and NH_3 plots a small feature at ~2340 cm^{-1} is attributed to the CO_2 purging instability in the IR-beam path, which becomes negligible for pure CO_2.

Table 4
List of parent and potential photoproduct species with their fragmented masses upon electron impact ionisation. The molecules are listed in order of increasing peak temperature per category.

Species	Primary m/z	Secondary m/z	$Temp_{peak}^{ref.}$ (K)	Ice matrix
Parent species				
CO_2	44	28	80[a]	Pure CO_2 on ASW
NH_3	17	16	105[a]	Pure NH_3 on ASW
H_2O	18	17	155[a]	Pure H_2O on ASW
Photoproducts				
O_2	32	16	35[a]	Pure O_2 on ASW
CO	28	12	35[a]	Pure CO on ASW
CO_3	60	–	–	–
O_3	48	–	55–90[b]	O/O_2 on N_2
H_2CO	29	30	110 & 147[c]	H_2O:H_2CO (6:1)
HNCO	43	42	130[d]	HNCO:$^{12}CH_4$ (1:1)
CH_3OH	31	32	~155[e]	H_2O:CH_3OH (7:1)
HCOOH	29	46	160[f]	H_2O:HCOOH (10:1)

Note. — Characteristic peak temperatures obtained from: [a]Minissale et al. (2022) for pure ices deposited on compact Amorphous Solid Water (ASW). [b]Minissale and Dulieu (2014). [c]Noble et al. (2012). [d]Ligterink et al. (2018). [e]Wolff et al. (2007). [f]Ioppolo et al. (2010). When multiple species have a mutual mass component, the secondary mass can be used to verify the assignment of a species for a given temperature peak.

Table 5
Measured IR bands at 15 K and 70 K for pure and mixed ices. Dashes indicate convoluted peaks for the ice mixture. The literature values for similar temperatures are listed in Table 3.

Species	Peak position (cm^{-1}) at **15 K**		Peak position (cm^{-1}) at **70 K**	
	Pure	Mixed	Pure	Mixed
H_2O	861	849	883	871
	1671	–	1671	–
	3411	–	3400	–
CO_2	2342	2357	2342	2342, 2377
	2376	–	2373, 2366[a]	–
	2387	–	2387	–
	3597	3588	3596	3596
	3705	3699	3705	3704
NH_3	1101	1116	1072, 1123, 1140	1113
	1631	–	1652	–
	3212[a], 3381	–	3207[a], 3381	–

Note. — [a]Denotes a shoulder feature.

such as the H_2O (ν_1) with NH_3 (ν_1/ν_3) between ~3100–3600 cm^{-1} and H_2O (ν_2) with NH_3 (ν_4) between ~1580–1720 cm^{-1}. Because of these overlaps we utilised water's ν_R and ammonia's ν_2 bands to calculate their column densities, unambiguously. The peak positions of the IR features are presented in Table 5.

We find that diluted CO_2 in an ice mixture at 15 K exhibits distinct differences compared to pure CO_2 ice (Fig. 4). In particular, the strongest IR feature of CO_2 at ~2340 cm^{-1} (Fig. 3(a)) is composed of a single peak at 2357 cm^{-1} at 15 K, whereas at 70 K the peak splits into one smaller peak near 2342 and a second, sharper feature at 2377 cm^{-1}. Additionally, both combination modes of CO_2, at ~3590 cm^{-1} and ~3700 cm^{-1}, become more distinct at higher temperatures (Fig. 3(b)). This observation corroborates prior experimental findings of mixed CO_2 (Blake et al., 1991; Ehrenfreund et al., 1999; Bernstein et al., 2005; Hodyss et al., 2008). The change of the bands' shape is explained by segregation, a process in which CO_2 molecules become sufficiently mobile to arrange themselves into groups of pure CO_2. In a study by He et al. (2017) for CO_2 on non-porous amorphous solid water ice, the required temperature was found to be 65 K, below which the diluted CO_2 molecules are trapped and cannot form clusters.

Another tool to assess segregation is through the shift of the peak position of an infrared absorption feature. In the tertiary ice mixture, the CO_2 combination modes for a tertiary ice at 15 K are redshifted by 6 to 9 cm^{-1}, compared to pure CO_2 ice at 15 K (see Table 5). At 70 K, no significant difference is observed between CO_2's combination modes in the pure and tertiary ice. However, the asymmetric stretching band exhibits a blueshift from 2373 cm^{-1} in the pure ice to 2377 cm^{-1} in the tertiary ice mixture. These results are consistent with the work from Bernstein et al. (2005) who report a similar wavelength blueshift and the local CO_2 concentration.

Lastly, we do not observe the OH-dangling mode observed near 3655 cm^{-1} at 70 K (Fig. 3(b)). Given that the dangling mode is an indicator for pore surface area, this discrepancy suggests a different ice structure possibly due to the gradual annealing of ice (Bernstein et al., 2005), opposed to our approach of depositing the ice at the same temperature as recording the IR spectrum. Thus, the formation history of ice mixtures could affect the ice structure and related IR features. Our findings on morphological changes in a mixed ice confirm that deposition at higher temperatures leads to CO_2 segregation.

3.2. Photon energy effect on H_2O:CO_2:NH_3 (2:1:1) ice mixture

3.2.1. Microwave-discharge hydrogen-flow lamp (6.9–10.8 eV; 115–180 nm)

Comparison of mid-infrared spectra during irradiation at 15 K vs. 70 K

IR spectra of H_2O:CO_2:NH_3 ice mixture obtained before and after MDHL photon irradiation for a fluence of 2.45×10^{18} photons cm^{-2} at 15 and 70 K are shown in Fig. 5(a). For 15 K (marked in blue),

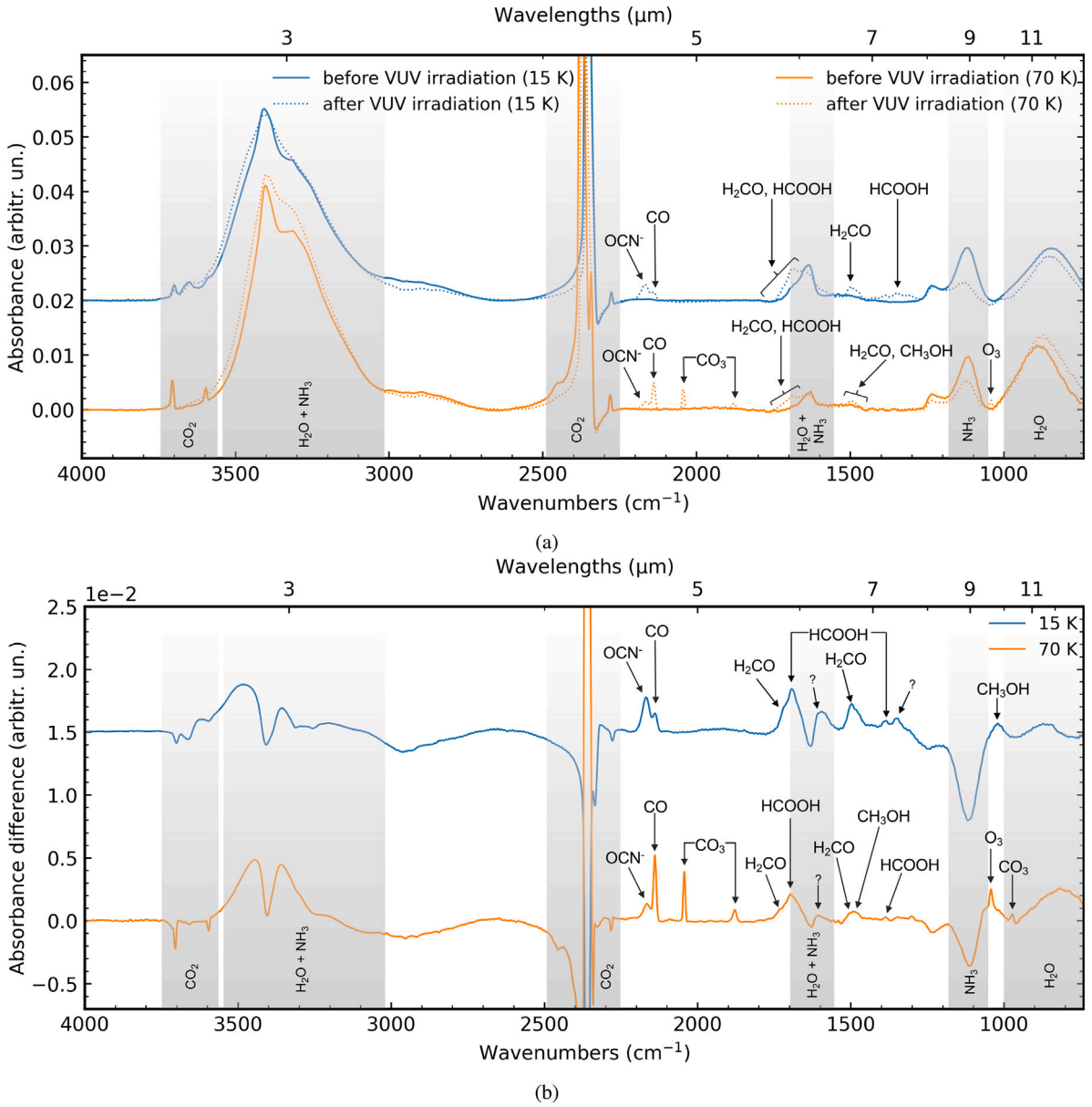

Fig. 5. (a) Mid-IR spectra after deposition (no fluence) and a maximum fluence of 2.45×10^{18} photons cm^{-2} and (b) difference spectra composed of spectra before and after VUV-irradiation of a $H_2O:CO_2:NH_3$ (2:1:1 ratio) at 15 K (blue) and 70 K (orange). Photoproducts are assigned with arrows and an offset between the plots is introduced for better visibility. To interpret the references to the colour references in this figure legend, the reader is directed to the web version of this article.

a substantial decrease of the peak absorbance values of the parent species due to photodissociation is also visible in Fig. 5(b) at certain wavelengths. Beyond this, increases are observed in other places. These new absorption features correspond to new species that are formed during irradiation. New peaks are assigned to corresponding vibrational transitions of cyanate ion (OCN^-) at 2168 cm^{-1}, carbon monoxide (CO) at 2138 cm^{-1}, formaldehyde (H_2CO) at 1495 cm^{-1}, and formic acid (HCOOH) at 1384 cm^{-1}. The vibration of the C = O stretching mode of H_2CO and/or HCOOH is ambiguous owing to the broad H_2O feature near 1670 cm^{-1}. However, in the difference spectrum in Fig. 5(b) the peaks at 1717 cm^{-1} and 1495 cm^{-1} become visible, confirming the detection of H_2CO and HCOOH, respectively. Further, we observed the formation of OCN^- becoming visible in the IR after a 15-min irradiation (fluence = 2.1×10^{17} photons cm^{-2}). The late onset of its formation suggests it is a second-generation species that is formed in these experiments (van Broekhuizen et al., 2005; Fedoseev et al., 2016). It is likely that HNCO is formed first, which has been proposed through an acid–base reaction with NH_3 (Raunier et al., 2004; van Broekhuizen et al., 2004). All observed values are in close agreement with the peak positions reported in the literature (see Table 6).

The negative blue peaks in Fig. 5(b) for NH_3 (1180 cm^{-1}, 1630 cm^{-1}), CO_2 (2360 cm^{-1}, 3700 cm^{-1}), and H_2O (762 cm^{-1}) imply a destruction of the parent species. This leads to the formation of radicals that diffuse and react in the ice, forming new species, appearing as positive IR peaks. In the overlapping H_2O/NH_3 region near ~3300 cm^{-1} a distinct dip is observed which is either owed to the change in physical structure of the ice, a decrease in column densities or a combination of both, thus altering the spectral shape of water and ammonia's stretching modes or lowering the absorbance of the absorption features, respectively. A structural reorganisation of the ice is possible: Leto and Baratta (2003) proposes the amorphisation of crystalline water ice due to Ly-α photon irradiation for ices below 70 K which applies to our experiment and may explain the changed spectral shape. Moreover, the CH_3OH band which is obscured by the water bending mode for

Table 6
Potential photoproducts after VUV-irradiation of a H_2O:CO_2:NH_3 tri-mixture according to the expected IR peak positions and TPD detection in the QMS. An ambiguous detection, denoted (✓), is explained further in the results section. Crosses imply that no photoproduct has been detected above the detection threshold. Question marks indicate unidentified species.

Potential photoproducts	15 K		70 K		Literature[ref.]
	Meas. peak position (cm^{-1})	QMS-TPD	Meas. peak position (cm^{-1})	TPD	(cm^{-1})
CO_3	–	✗	971	✗	972[a]
O_3	–	✗	1043	✓	1045[b]
CH_3OH	1019	✓	–	✓	1026[c]
Unidentified	1345	–	–	–	–
HCOOH	1384	✓	1386	✗	1384[d]
CH_3OH	–	✓	1456	✓	1459[d]
H_2CO	1495	✓	1491	✓	1496[e]
Unidentified	1596	–	1606	–	–
HCOOH	1694	✓	1694	✗	1695[f]
H_2CO	1717	✓	1716	✓	1719[e]
CO_3	–	✗	1878	✗	1879[a]
CO_3	–	✗	2043	✗	2044[a]
CO	2138	(✓)	2138	(✓)	2139[d], 2140[g]
OCN^-	2168	✓	2166	✓	2166[h], 2164[g]

Note. — [a]Bennett et al. (2004). [b]Brewer and Wang (1972). [c]Hudgins et al. (1993). [d]Bouilloud et al. (2015). [e]Schutte et al. (1993). [f]Bisschop et al. (2007). [g]Bossa et al. (2008). [h]van Broekhuizen et al. (2005).

15 K in Fig. 5(a) appears at 1019 cm^{-1} in the blue difference spectrum (Fig. 5(b)), in good agreement with the literature value at 1026 cm^{-1} (Hudgins et al., 1993).

For characteristic temperatures at Enceladus' surface near 70 K, we present the infrared spectra in orange for tertiary ices before and after irradiating the ice with the MDHL in Fig. 5(a). The new species compared to those also detected in the irradiation experiment at 15 K are ozone, O_3 (1043 cm^{-1}), and carbon trioxide, CO_3 (971, 1878, 2043 cm^{-1}). The spectral positions of the previously detected photoproducts at 70 K are 2138 cm^{-1} for CO, 2166 cm^{-1} for OCN^-, 1491 and 1716 cm^{-1} for H_2CO, 1386 and 1694 cm^{-1} for HCOOH, and 1456 cm^{-1} for CH_3OH. A peak for O_3 appears at 1043 cm^{-1} in good agreement with the literature value at 1045 cm^{-1} (Brewer and Wang, 1972). CO_3 is also clearly identified in the infrared spectrum: While the infrared spectrum for 70 K in Fig. 5(a) displays two of the characteristic bands at 1878 and 2043 cm^{-1}, a third peak becomes visible peaks in the corresponding difference spectrum (Fig. 5(b)) at 971 cm^{-1}. These values agree very well with the literature values within 1 cm^{-1} (see Table 6).

The detection is further verified by a control experiment of irradiated pure CO_2 ice. The mid-IR spectrum before and after irradiation (Fig. A.1 in Appendix A) shows the same bands as well as the C-O stretch. band of CO_3 at 972 cm^{-1} (Bennett et al., 2004), which is obscured by the water libration mode for 70 K in the tertiary mixture (Fig. 5(a) while visible in Fig. 5(b)) or in a H_2O:CO_2 ice mixture (Fig. B.1 in Appendix B). In this control experiment ozone was also detected, implying that the formation of CO_3 and O_3 relies on the photodissociation of CO_2 into CO + O and subsequent diffusion reaction of those photofragments or, alternatively, through O-atom addition reactions to CO_2.

Fig. 6 displays the evolution of the abundance of CO_2 and NH_3 with fluence, based on the measured column densities of the respective IR bands at 3704 cm^{-1} and at 1113 cm^{-1}. Assuming zero-order kinetics, an exponential decay fit (Eq. (4)) allows determining the photodestruction cross-sections for CO_2 and NH_3, resulting in $\sigma_{CO_2} = (1.43 \pm 0.01) \times 10^{-19}$ cm^2 and $\sigma_{NH_3} = (2.99 \pm 0.1) \times 10^{-19}$ cm^2. The obtained photodestruction cross-sections agree, within a factor of a few, with literature values of $\sigma_{NH_3} = (7.1 \pm 1.2) \times 10^{-19}$ cm^2 (Chuang et al., 2024) and $\sigma_{CO_2} = 3.8 \times 10^{-19}$ cm^2. Due to the scarcity of available data for the CO_2 photodestruction cross-sections, we estimated σ_{CO_2} using the following equation, assuming complete absorption of incident photons by the ice:

$$\sigma_{CO_2} = \sigma_a \times G_{UV}, \tag{3}$$

where $\sigma_a = 6.7^{+0.5}_{-0.9} \times 10^{-19}$ cm^2 is the known CO_2 photoabsorption cross-section (Cruz-Diaz et al., 2014) and $G_{UV} = 0.56 \pm 0.09$ is the CO_2 photodestruction yield reported by Gerakines et al. (2000). Further, it is well known that the photodissociation efficiency (quantum yield) and differences in the ice temperature or photon energy can affect the photolysis cross-section values (Schmidt et al., 2013; Cruz-Diaz et al., 2014).

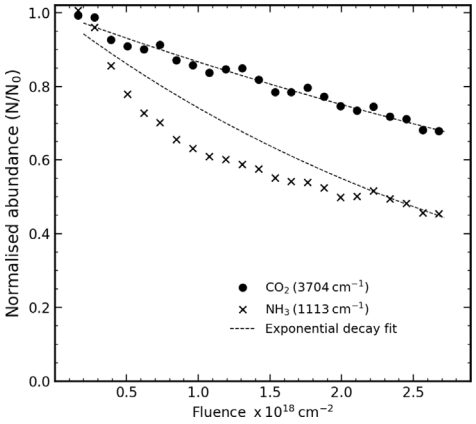

Fig. 6. The normalised molecular abundance, or fraction of remaining parent molecules, in a tertiary ice mixture at 70 K with fluence.

$$\frac{N_t}{N_0} = e^{-\sigma \times \phi \times t} \tag{4}$$

where t is the time since the irradiation start in seconds, N_t is the molecular abundance at a certain irradiation time in molecules cm^{-2}, N_0 is the initial molecular abundance at t = 0 s, σ is the photodestruction cross-section in cm^2, and ϕ is the VUV flux in photons cm^{-2} s^{-1}. For water ice, due to the low detector sensitivity near the wavelength range cut-off, the uncertainty for the water libration mode is deemed insufficient to derive a meaningful photodestruction cross-sections. The determined photodestruction cross-section values are then used to calculate the molecular survival times in seconds, or half-life, with Eq. (5). Therefrom, a molecular half-life for CO_2 and NH_3 of $t_{1/2} = 5.9$ h and $t_{1/2} = 2.8$ h under laboratory conditions is found, respectively.

$$t_{1/2} = \frac{ln(2)}{\sigma \times \phi \times t} \tag{5}$$

Comparison of TPD for tertiary ices irradiated at 15 and 70 K

We report the QMS signal of photoproducts during the TPD experiment for irradiated tertiary ices at 15 and 70 K, as shown in Fig.

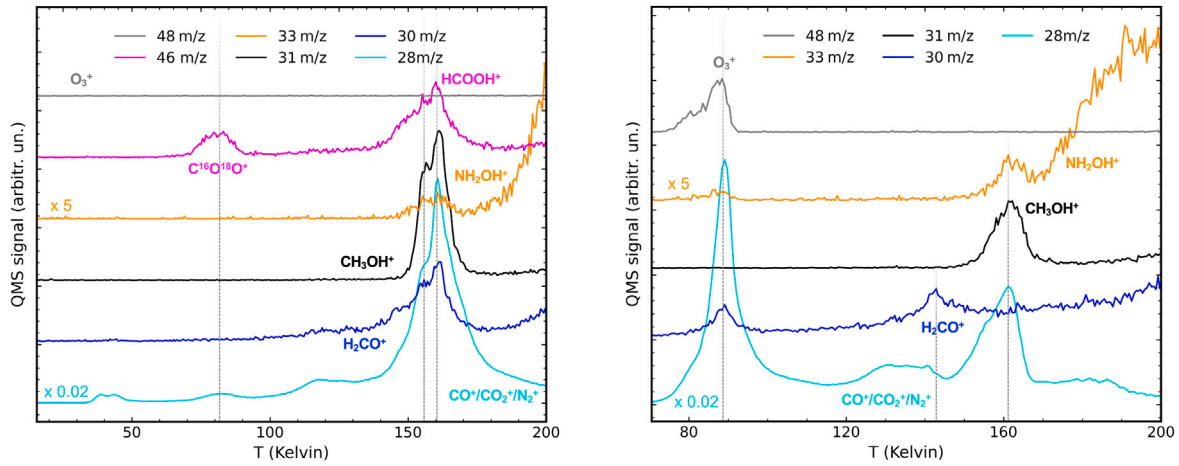

(a) TPD from 15 to 200 K.

(b) TPD from 70 to 200 K.

Fig. 7. Ion mass fragment (m/z) of photoproducts during TPD of a $H_2O{:}CO_2{:}NH_3$ ice mixture irradiated at (a) 15 K and (b) 70 K. TPD profiles are offset and in some cases scaled for clarity.

7. The dashed lines indicate several desorption peaks of the detected species. The photoproducts are identified according to their characteristic desorption peaks and m/z values, which were carefully selected to represent the primary or secondary fragmented mass as summarised in Table 4.

The QMS-TPD data of tertiary ice irradiated at 15 K (Fig. 7(a)) shows the volcano desorption of entrapped HCOOH, OCN^-, CH_3OH, H_2CO, CO/CO_2 and NH_2OH in water ice at ~155 K and 161 K, consistent with the expected temperatures for the structural changes (shoulder of QMS signal) and peak desorption of water ice, respectively. The peak at ~160 K also correlates well with the predicted disappearance of the IR peaks of HCOOH, although volcano desorption with water at this temperature or a combination of both desorption mechanisms cannot be ruled out. While a signal for $m/z = 33$ (NH_2OH^+) appears near 160 K, it is weaker than for 70 K with no signal detected near 80 K, unlike a small bump seen in Fig. 7(a) for $m/z = 33$. To this end, the assignment of NH_2OH is only tentative. The small quantity may explain why it is not seen in the IR difference spectrum in Fig. 5(b) for 15 K. Note that the QMS-TPD data at temperatures above 150 K may contain signal bleeding, and thus, adds some uncertainty to the measurements above these temperatures. Carbon monoxide's signature in the QMS-TPD data of CO^+ ($m/z = 28$) is either attributed to newly formed CO or a fragment of CO_2. However, the detection of CO is corroborated as a result of its matching IR band. OCN^- ($m/z = 42$) is not included in Fig. 7, albeit being detected the QMS-TPD data, as it is a well-known product from $H_2O - NH_3$ photochemistry and its identification is already confirmed by its characteristic IR signature (Fig. 5). Fig. 7(b) presents the QMS-TPD data obtained for the tertiary ice irradiated at 70 K, and subsequently being warmed to 200 K. Similarly to the 15 K experiment, the detected species are OCN^-, CH_3OH, H_2CO and CO/CO_2, albeit no QMS signal for HCOOH is observed near its characteristic desorption temperature. Most notably, new QMS traces appear for ozone, O_3^+ and hydroxylamine, NH_2OH^+. A clear peak is visible for O_3^+ ($m/z = 48$) at 88 K, which falls within the expected desorption range of 50–90 K (Minissale and Dulieu, 2014). For H_2CO, the desorption peak shifts from a higher to a lower desorption temperature compared to the TPD for the 15 K (Fig. 7(a)). This may be due to a higher abundance of H_2CO in the ice mixture irradiated at 70 K. Thus, the molecules can find each other and collectively desorb closer to the characteristic desorption temperature (~147 K) instead of volcano-desorbing with water. For hydroxylamine ($m/z = 33$), one peak appears near ~160 K, most likely due to H_2O volcano desorption at this temperature. A second, stronger signal increase is recorded from ~170 K to ~200 K, the highest recorded TPD temperature.

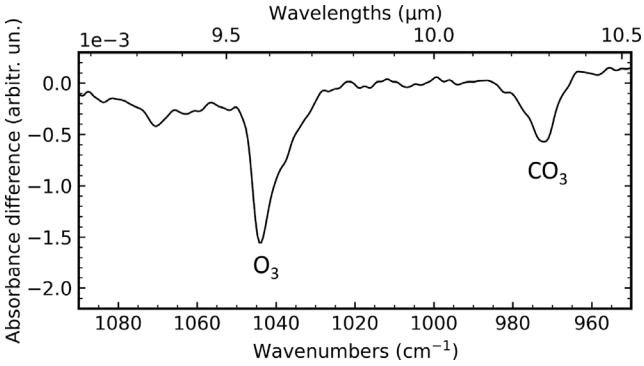

Fig. 8. Difference IR spectrum between 77–93 K showing the disappearance of the O_3 (1043 cm^{-1}) and CO_3 band (972 cm^{-1}) in a $H_2O{:}CO_2{:}NH_3$ ice mixture irradiated at 70 K.

Difference IR spectra during the TPD

Lastly, TPD tailored difference spectra can be used to further identify photoproducts by comparing the disappearance of IR bands during TPD to the simultaneous increase of mass signatures associated with a species in the QMS data. Hereby, the difference IR spectrum is created using two spectra corresponding to the upper and lower limit of a temperature range seen in the QMS-TPD data, opposed to spectra taken before and after irradiation.

For the irradiated $H_2O{:}CO_2{:}NH_3$ ice mixture at 70 K, the negatives peaks in Fig. 8 give additional evidence for thermal desorption of ozone and carbon trioxide by showing the disappearance of the expected IR band at 1043 cm^{-1} from 77–93 K during TPD.

The desorption temperature range of CO_3 is precised to 82–93 K, as shown by two other characteristic bands at 1878 and 2043 cm^{-1} simultaneously disappearing in Fig. D.1 (Appendix D). While the spectral positions for all the peaks are in close agreement with the literature values for CO_3 given by Bennett et al. (2004) (see Table 6). In contrast, no peak appears in the QMS-TPD data for the expected m/z of 60 in this temperature range. CO_3 may have fragmented during impact ionisation before a possible detection in the QMS. However, the fragmentation pattern of CO_3 is not available. Nonetheless, due to the observed simultaneous formation, photodestruction and disappearance for both aforementioned peaks, we suggest the presence of CO_3 in our tri-mixture.

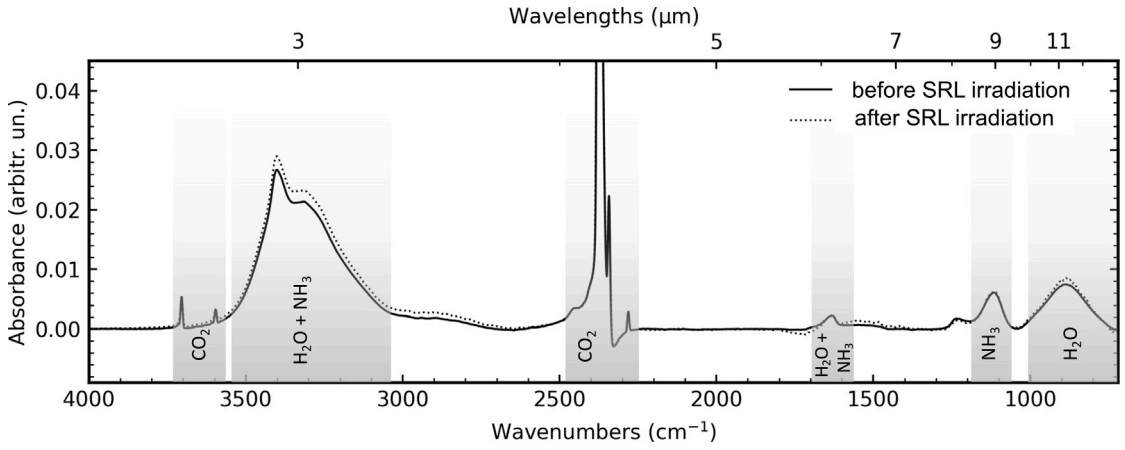

Fig. 9. The infrared spectra of $H_2O:CO_2:NH_3$ (2:1:1 ratio) ice after deposition and a 3 h long irradiation with the SRL.

Further, we tentatively assign NH_2OH as a photoproduct in the ice mixture. The mass signal $m/z = 33$ characteristic for NH_2OH^+ was recorded as shown in Fig. 7(b). This peak correlates with the disappearance of four characteristic peaks at 928, 1201, 1375, and 3315 cm^{-1} in the difference IR spectrum during TPD in Fig. D.2 (Appendix D), in close agreement with the spectral positions reported in the literature (Table D.1). Additionally, a control experiment of the VUV-photolysis of a H_2O : NH_3 mixture was performed (Table C.1, Fig. C.1 in Appendix C). The majority of the IR bands are in agreement with respect to the $H_2O:CO_2:NH_3$ results. Hydroxylamine's mass signature of $m/z = 33$ peaks within a similar temperature range of 172 to 221 K to that found in other experiments (~165–225 K in Fedoseev et al. (2016)), although the TPD for the tri-mixture was not recorded above ~200 K. The detection of H_2CO is further confirmed by the characteristic spectral peaks seen in the difference spectrum for the TPD range from 110–142 K (Table D.1). The aforementioned photoproducts are summarised in Table 6 based on the QMS-TPD results as well as IR data collected during VUV-irradiation.

3.2.2. Solar radiation lamp (0.7–6.2 eV; 200–1800 nm)

We performed an irradiation experiment with the SRL to compare our results to the above VUV-irradiation experiment in order to understand the photon energy effect on ice chemistry. The mid-IR spectra of $H_2O:CO_2:NH_3$ mixed ice obtained before and after the SRL-photon irradiation for a fluence of $\sim 2 \times 10^{19}$ photons cm^{-2} at 70 K are presented in Fig. 9. As can be seen, no new IR features corresponding to photoproducts were detected due to the SED of the SRL. Although the radiation source covers the higher end of the photon energy range, its SED displayed in Fig. 2(b) is such that the majority of photons are emitted within the visible and near-infrared wavelength range above ~380 nm or below 3.3 eV. These energies are below the bond dissociation energies required to break the chemical bonds of all three parent species. For example, the covalent C = O bond of CO_2 requires photons with energies ≥5.5 eV. Therefore, we do not expect photons with energies characteristic for the SRL to induce photodissociation processes nor ice chemistry in similar ice mixtures. The same behaviour is observed at 15 K (i.e., the infrared spectra from Fig. 3 remains unchanged) and is not discussed here further. The slight increase in IR features of the parent species (i.e., ~10% increase in absorbance area) can be attributed to residual background deposition over the duration of the experiment. In summary, no photoproducts were detected with the SRL. Therefore, the rest of the photochemistry experiments in this work were performed using solely the MDHL lamp.

3.3. Discussion

Our experiments show that the photochemistry of irradiated $H_2O:CO_2:NH_3$ ice mixtures differs between low (15 K) and high temperatures (70 K). At 15 K, we found evidence for the formation of carbon monoxide, cyanate ion, formaldehyde, formic acid, and methanol. The most striking result is the detection of CO_3 and O_3 at 70 K, corroborated by the aforementioned IR and QMS signals in addition to the above photoproducts at 15 K. Further, we tentatively identified NH_2OH.

Eqs. (6)–(8) describe the widely accepted photodissociation pathways of the parent species H_2O (Tanaka et al., 1961; Stief et al., 1975), CO_2 (Okabe et al., 1978; Öberg et al., 2009b; Martín-Doménech et al., 2015) and NH_3 (Gerakines et al., 1996; Loeffler and Baragiola, 2010):

$$H_2O + h\nu \rightarrow OH + H \quad (6)$$

$$CO_2 + h\nu \rightarrow CO + O \quad (7)$$

$$NH_3 + h\nu \rightarrow NH_2^{\cdot} + H \quad (8)$$

The detected photoproducts described in Section 3 can be explained by reactions between radicals, ions and the molecules in the ice, facilitated by photodissociation of the parent species. Thus, H_2CO can form through hydrogenation of CO from dissociated CO_2 (Eq. (7)) with subsequent hydrogenation forming CH_3OH (Watanabe and Kouchi, 2002). Furthermore, the intermediate HCO radicals can react with OH radicals forming HCOOH. CO acts as another precursor when reacting with the NH_2 radical, resulting in HNCO + H. Consequently, HNCO reacts with surrounding NH_3 molecules through an acid–base reaction, leading to the formation of OCN^- and NH_4^+ (Demyk et al., 1998; van Broekhuizen et al., 2004).

The formation of hydroxylamine may be due to the photodissociation of NH_3 (Eq. (8)) and recombination with OH as proposed by Zheng and Kaiser (2010) for an electron irradiated water-ammonia ice.

$$NH_2 + OH \rightarrow NH_2OH \quad (9)$$

Ozone is likely formed from photodissociation of CO_2 (Eq. (7)) and consecutive O atom addition (Eqs. (10), (11)):

$$O + O \rightarrow O_2 \quad (10)$$

$$O_2 + O \rightarrow O_3 \quad (11)$$

For carbon trioxide, the formation mechanism is expected to occur through O atom addition to the readily available CO_2 (Eq. (12)).

$$CO_2 + O \rightarrow CO_3 \quad (12)$$

In our control experiment of irradiated pure CO_2 ice we observed the formation of CO, O_3 and CO_3 (Appendix A), confirming the proposed reaction pathway based on the sole precursor CO_2 (Eqs. (7)–(12)).

One reason why oxygen-bearing photoproducts such as CO_3 and O_3 dominate over hydrogen-bearing photoproducts at elevated temperatures is the desorption of atomic/molecular hydrogen at lower temperatures (~15 K) w.r.t. atomic oxygen (~50 K). Thus, hydrogenation dominates at lower temperatures, while the enhanced mobility of species at elevated temperatures leads to a higher collision rate of reactants on the surface and in the bulk of the ice (Cuppen et al., 2017).

4. Application to Enceladus and other icy moons

The main result of our experimental work suggests that UV-photolysis of Enceladus' ice analogues enriched in CO_2 leads to the formation of solid-state ozone and carbon trioxide at 70 K compared to ISM-like temperatures at 15 K. We experimentally observe the UV-induced formation of ozone in a water-carbon dioxide ice matrix based on its asymmetric stretching mode at 1043 cm^{-1}. Ozone remains in the solid state below 88 K, whereafter it sublimates as revealed by our QMS-TPD data peak for the ozone ion (m/z = 48) at typical peak desorption temperatures.

Therefore, our results give evidence that solid-state ozone should be present on Enceladus' surface at temperatures below 88 K. At higher daytime temperatures such as those found on other icy saturnian satellites (e.g., ~130–140 K for Hyperion, ≥100 K for Mimas (Filacchione et al., 2016)), ozone is expected to be released into the atmosphere. A non-detection of ozone on Enceladus to date does not discard its presence, considering Cassini's instruments were unable to detect the most prominent O_3 bands (i.e., the 240–300 nm Hartley band, 1043 cm^{-1} mid-IR band) due to not covering the required wavelength range or low SNR of the spectrometers. Moreover, the ozone cation (O_3^+) was not detected by the Ion and Neutral Mass Spectrometer (INMS) aboard Cassini (Magee and Waite, 2017; Khawaja et al., 2019), possibly attributed to the insufficient mass resolution and sensitivity of the mass spectrometer to disentangle fragmented molecules produced from the high particle impact speeds.

On Enceladus, pure CO_2 has been detected by Cassini's VIMS instrument between the tiger stripes (Combe et al., 2019) with temperatures remaining below 80 K (CIRS, Abramov and Spencer (2009)). Matson et al. (2018) postulates that CO_2 originates from the ocean, whereby CO_2 seeping through the crust and freezing out on the cold surface is responsible for its pure concentration. Thus, the regions between the tiger stripes offer suitable conditions for the formation of ozone in the surface ice, after gardening (e.g., photolysis, radiolysis) of concentrated CO_2 ice. Our study suggests the presence of endogenic ozone trapped in the surface ice at the characteristic temperatures between the tiger stripes.

On the other hand, at Ganymede, a study by Noll et al. (1996) linked the broadening and slight red-shifting of the Hartley band to gas-phase ozone being trapped in cracks and voids within the surface ice. Recently, JWST observations revealed that solid state CO_2 is spread across the entire surface of Ganymede with lower abundances at the poles, where CO_2 is mixed with water ice. At lower latitudes, CO_2 could be trapped in non-icy material such as minerals and salts, which were seen as darker regions (Bockelee-Morvan et al., 2024). Our study suggests that the ozone formed at the poles due to energetic processes would not be stable at these temperatures (~140 K). The observed trapped ozone from Noll et al. (1996) could then be attributed to CO_2 processed at lower latitudes, where ozone probably desorbs into gas pockets and remains trapped in the surface material. On Rhea and Dione, O_3 is also found in the surface (Noll et al., 1997), where average temperatures remain below those of the Galilaen satellites (<80 K; Teolis and Waite (2016)). This agrees with our experimental finding of trapped ozone in a water-rich CO_2 ice at temperatures <88 K. Furthermore, the detection of an O_2-CO_2 exosphere (Teolis et al., 2010; Teolis and Waite, 2016) from radiolysis, photolysis or impact sublimation suggests the presence of solid-state O_2 and CO_2, confirmed by VIMS observations of Rhea and Dione (Stephan et al., 2010, 2012).

We showed that CO_2 gardening is a key building block for O_3 formation which appears to be a common process on several icy moons across the Solar System, supported by the aforementioned observations and laboratory results. Although past experimental studies have demonstrated the formation of ozone through 5 keV electron bombardment of pure oxygen ice at 11 - 30 K (Bennett and Kaiser, 2005; Sivaraman et al., 2007) or proton radiolysis of oxygen mixed with water ice at 80 K (Moore and Hudson, 2000), our study is the first to examine the UV-photolysis of Enceladus-like ices enriched in CO_2 at the same deposition and irradiation temperature of 70 K. Future spaceborne instrumentation exploring the surfaces of icy moons must be fine-tuned to confirm the presence and physico-chemical state of ozone and other O-bearing species such as CO_3. Thereby, high-resolution spectrometers searching for trapped ozone in the ice matrix must be able to measure broadly spaced absorption bands in the UV (240–300 nm) and mid-IR regions (1043 cm^{-1}), as well as those for solid carbon trioxide (971, 1878, 2043 cm^{-1}). For in-situ detection of ozone, the impact velocity of molecules governed by the in-situ sampling speed must be sufficiently low to avoid excessive fragmentation of molecules in mass spectrometers and false positives from artificial synthesis of new species (Martins et al., 2013; New et al., 2021). Furthermore, a high mass resolution compared to that of Cassini's INMS (Δm = 1 amu) is required to disentangle ambiguous mass peaks (Magee and Waite, 2017).

Building on our findings of the new photoproducts, questions concerning their survivability and implicit detectability naturally arise. The reported photodestruction cross-sections of CO_2 and NH_3 in Section 3.2.1 are extrapolated to geologically relevant timescales at Enceladus, given the known laboratory-to-Enceladus energy flux scaling (Table 1). Therefrom, we derive half-lives for CO_2 and NH_3 ice on Enceladus of ~11 and ~5 days, respectively. Hereby, possible replenishing processes such as gas seeping through the icy crust (Combe et al., 2019) may be responsible for the survivability not only of these parent species but also the detected photoproducts, whereby the replenishing rate must be equal or greater than the destruction rate. Vice versa, future observations of these photoproducts such as ozone, carbon trioxide or cyanate ion may hint at ongoing replenishing processes, considering the building blocks for the photoproducts formation are required from a separate source.

5. Summary and conclusions

We experimentally studied the photochemistry of irradiated ice mixtures (H_2O, CO_2, and NH_3) under ultra-high vacuum conditions using vacuum-ultraviolet (VUV) radiation and solar radiation to determine chemical reactions and their products. To our knowledge, this is the first systematic study investigating the effect of VUV/Vis radiation on the chemical composition of Enceladean ice analogues at temperatures relevant for Enceladus (70 K), with a comparison to ISM conditions (15 K). Our findings are the following:

- Photon Energy Effects: VUV photons (MDHL) induce significant chemical changes, leading to the formation of various organic and inorganic compounds. SRL photons, with lower energies, did not induce chemical evolution above the detection threshold, suggesting that VUV photons (6.9–10.8 eV in this work) are most responsible for ice chemistry.
- Temperature Effects: At 15 K, photoproducts such as carbon monoxide (CO), cyanate ion (OCN^-), formaldehyde (H_2CO), methanol (CH_3OH) and formic acid (HCOOH) were observed. At 70 K, additional products were detected, including ozone (O_3) and carbon trioxide (CO_3), due to a higher mobility of oxygen atoms and CO_2 segregation.
- Ozone is likely formed through O atom addition reactions in CO_2-rich ice regions and is potentially trapped on Enceladus' surface below 88 K.

- The estimated half-life of solid-state CO_2 and NH_3 on the surface of Enceladus is ~11 and ~5 days, respectively, suggesting an ongoing replenishing process.

The study demonstrates that photochemistry involving CO_2, H_2O, and NH_3 at different temperatures plays a central role in forming O-bearing molecules on icy bodies such as Enceladus. Understanding this photochemical process not only enhances our knowledge of icy moons' surface chemistry, but also of extraterrestrial environments and the potential habitability of ocean worlds in our Solar System.

CRediT authorship contribution statement

T.-M. Bründl: Writing – review & editing, Writing – original draft, Visualization, Validation, Methodology, Investigation, Formal analysis, Data curation, Conceptualization. **J. Terwisscha van Scheltinga:** Writing – review & editing, Writing – original draft, Supervision, Methodology, Investigation, Conceptualization. **S. Cazaux:** Writing – review & editing, Writing – original draft, Supervision, Funding acquisition, Conceptualization. **K.-J. Chuang:** Writing – review & editing, Writing – original draft, Methodology, Investigation, Conceptualization. **H. Linnartz:** Writing – original draft, Supervision, Resources, Funding acquisition, Conceptualization.

Declaration of competing interest

The authors declare that they have no known competing financial interests or personal relationships that could have appeared to influence the work reported in this paper.

Acknowledgements

In Memoriam of Prof. Harold Linnartz without whom this research would not have been possible: From giving access to his laboratory at the LfA to his valuable guidance on ice chemistry during numerous discussions. The authors thank the two anonymous reviewers for their helpful comments and recommendations. This work received funding from the Dutch Research Council (NWO) and contributes to the second round of the Planetary and ExoPlanetary Science Program (PEPSci-II).

Appendix A. Control experiment: Pure CO_2 ice (70 K)

See Fig. A.1.

Appendix B. Control experiment: H_2O : CO_2 ice mixture (70 K)

See Fig. B.1.

Appendix C. Control experiment: H_2O : NH_3 ice mixture (70 K)

The irradiation of a H_2O : NH_3 (8:2) bi-mixture was performed to facilitate the identification of photoproducts in a more complex ice mixture, described in Section 3.2.1. In particular, measurements of the QMS and infrared spectra were compared during TPD to unambiguously identify species due to the thermal desorption of species that would otherwise overlap with other species' IR bands or QMS desorption peaks. Table C.1 lists the assigned photoproduct, according to characteristic IR bands disappearing within a temperature range. Fig. C.1(a) evidences the disappearance of those IR bands in a difference spectrum, while C.1(b) displays the characteristic mass fragment peaking during the same temperature range in the QMS.

Appendix D. H_2O : CO_2 : NH_3 ice mixture (70 K)

See Figs. D.1, D.2 and Table D.1.

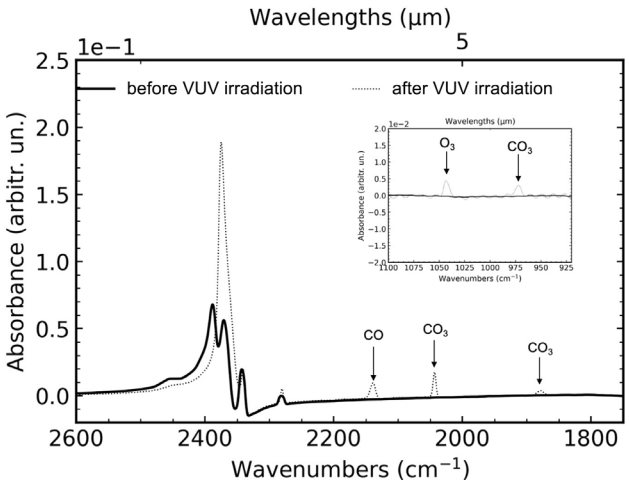

Fig. A.1. The mid-IR spectrum of pure CO_2 ice at 70 K before and after a maximum fluence of VUV-photolysis. The specifications of the ice can be found in Table 2.

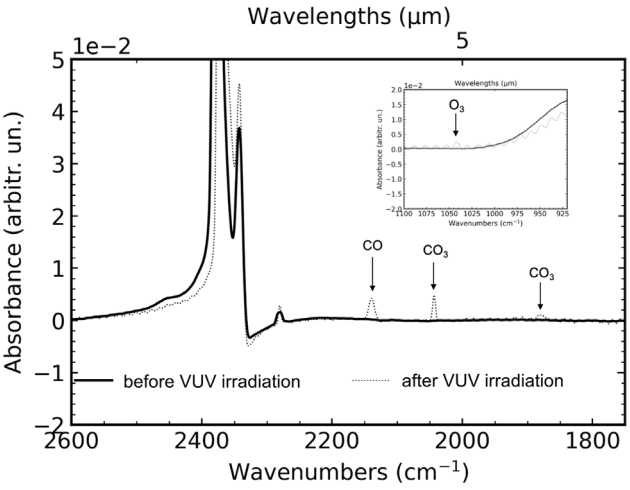

Fig. B.1. The mid-IR spectrum of a H_2O : CO_2 ice mixture before irradiation and a total fluence of 2.45×10^{18} photons cm^{-2}. It is noted that the CO_3 band at 972 cm^{-1} is obscured by water's broad libration mode peaking at 894 cm^{-1}. The specifications of the ice can be found in Table 2.

Table C.1
Characteristic parameters for NH_2OH forming during photolysis of a H_2O:NH_3 (8:2) ice mixture at 70 K. The observed and expected infrared bands are compared. Secondly, the mass fragments (m/z) that clearly correlate with the disappearance of the infrared band for a given temperature range are also given.

Photoproduct	m/z	$Temp._{desorb}$ (K)	Measured spectral range (cm^{-1})	Expected spectral range[references] (cm^{-1})
NH_2OH	33	172–221	892	895[b]
			919	919[a]
			1206	1203[a]
			1367	1359[a]
			2898	2899[a]
			3264	3261[a]
			3312	3317[a]

Note. — [a]Congiu et al. (2012). [b]Yeo and Ford (1990).

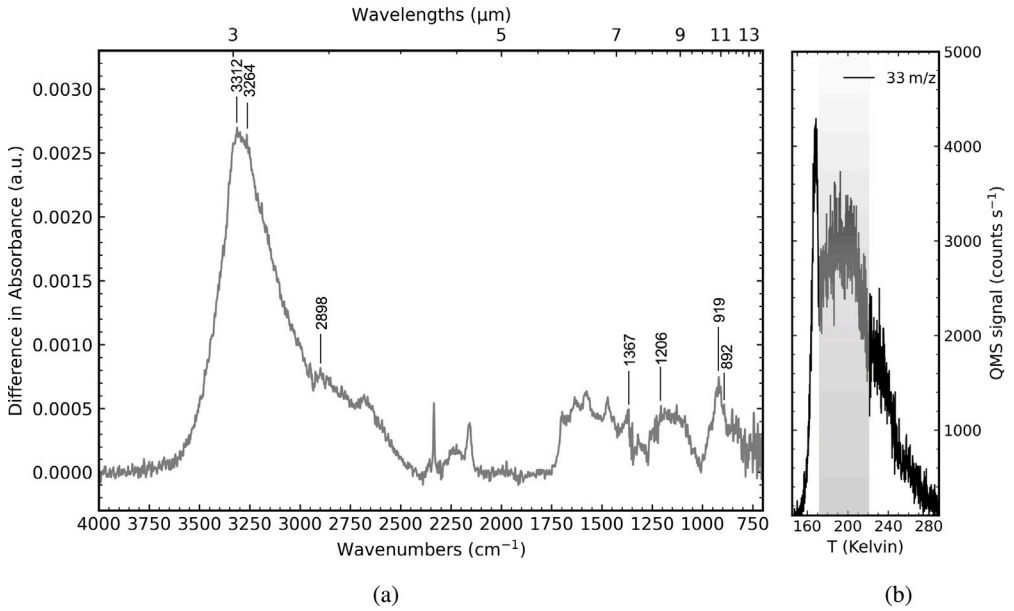

Fig. C.1. (a) The baseline corrected difference spectrum of the H_2O : NH_3 ice mixture detailed in Table 2 represents the absorbance difference between spectra taken at 172 and 221 K during TPD, whereby the spectral position for NH_2OH are marked and listed in Table C.1. (b) The QMS data for m/z = 33, showing an increased intensity between 172 and 221 K highlighted in the grey area, corresponds to NH_2OH^+. The sharp peak at ~170 K is due to the desorption of NH_3, which traps NH_2OH molecules in the ice matrix and releases them from the ice during desorption.

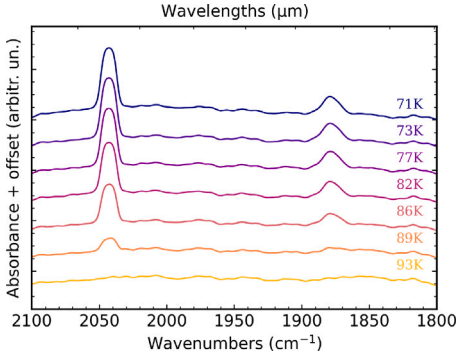

Fig. D.1. Two mid-IR peaks, assigned to CO_3, disappear simultaneously between 82 K and 93 K, confirming the desorption of the same species from the VUV-irradiated tertiary ice mixture.

Table D.1
TPD: Assignment of potential photoproducts according to disappearing IR absorption bands within a given temperature range during TPD.

Photoproduct	m/z	Temp.$_{desorb}$ (K)	Measured spectral range (cm^{-1})	Expected spectral range^{references} (cm^{-1})
H_2CO	30	110–142	1240	1245[a]
			1498	1496[a]
			1721	1719[a]
NH_2OH	33	170–196	928	919[b]
			1201	1203[b]
			1375	1359[b]
			3315	3317[b]

Note.— [a]Schutte et al. (1993). [b]Congiu et al. (2012).

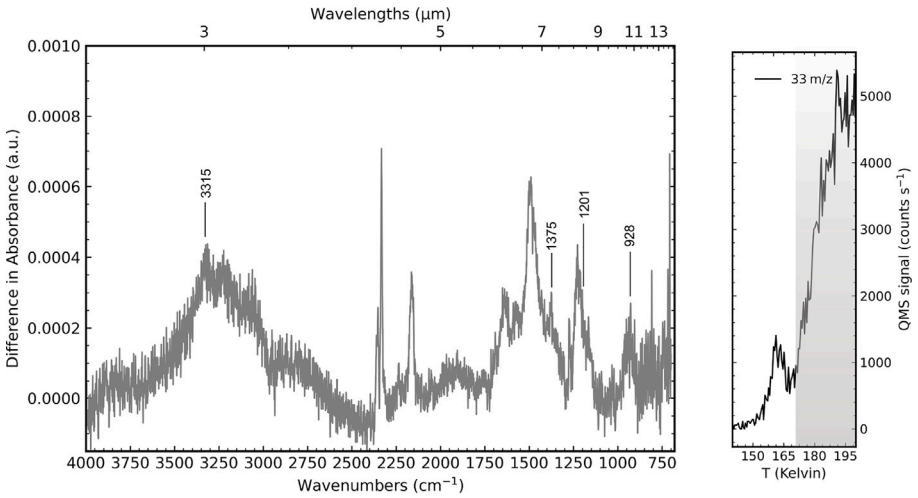

Fig. D.2. (a) The baseline corrected difference spectrum of the H_2O:CO_2:NH_3 ice mixture detailed in Table 2 represents the absorbance difference between spectra taken between 170 and 196 K during TPD. (b) The QMS data for m/z = 33, showing an increased intensity between 170 and 196 K highlighted in the grey area, corresponds to NH_2OH^+. The smaller peak at ∼161 K is due to volcano desorption of trapped NH_2OH molecules in the H_2O ice matrix.

Data availability

Data will be made available on request.

References

Abramov, O., Spencer, J.R., 2009. Endogenic heat from Enceladus' south polar fractures: New observations, and models of conductive surface heating. Icarus 199 (1), 189–196. http://dx.doi.org/10.1016/j.icarus.2008.07.016.

Baratta, G.A., Palumbo, M.E., 1998. Infrared optical constants of CO and CO_2 thin icy films. J. Opt. Soc. Amer. A 15 (12), 3076–3085. http://dx.doi.org/10.1364/JOSAA.15.003076.

Baratta, G.A., Palumbo, M.E., Strazzulla, G., 2000. Laboratory and astronomical IR spectra: An experimental clue for their comparison. Astron. Astrophys. 357, 1045–1050.

Bennett, C.J., Jamieson, C., Mebel, A.M., Kaiser, R.I., 2004. Untangling the formation of the cyclic carbon trioxide isomer in low temperature carbon dioxide ices. Phys. Chem. Chem. Phys. 6 (4), 735–746.

Bennett, C.J., Kaiser, R.I., 2005. Laboratory studies on the formation of ozone (O_3) on icy satellites and on interstellar and cometary ices. Astrophys. J. 635 (2), 1362–1369. http://dx.doi.org/10.1086/497618.

Bernstein, M.P., Cruikshank, D.P., Sandford, S.A., 2005. Near-infrared laboratory spectra of solid H_2O/CO_2 and CH_3OH/CO_2 ice mixtures. Icarus 179 (2), 527–534. http://dx.doi.org/10.1016/j.icarus.2005.07.009.

Bernstein, M.P., Dworkin, J.P., Sandford, S.A., Cooper, G.W., Allamandola, L.J., 2002. Racemic amino acids from the ultraviolet photolysis of interstellar ice analogues. Nature 416 (6879), 401–403.

Bisschop, S., Fuchs, G., Boogert, A., van Dishoeck, E., Linnartz, H., 2007. Infrared spectroscopy of HCOOH in interstellar ice analogues. Astron. Astrophys. 470 (2), 749–759.

Blake, D., Allamandola, L., Sandford, S., Hudgins, D., Freund, F., 1991. Clathrate hydrate formation in amorphous cometary ice analogs in vacuo. Science 254 (5031), 548–551.

Bockelee-Morvan, D., Lellouch, E., Poch, O., Quirico, E., Cazaux, S., de Pater, I., Fouchet, T., Fry, P., Rodriguez-Ovalle, P., Tosi, F., et al., 2024. Composition and thermal properties of Ganymede's surface from JWST/NIRSpec and MIRI observations. Astron. Astrophys. 681, A27.

Bossa, J.B., Theulé, P., Duvernay, F., Borget, F., Chiavassa, T., 2008. Carbamic acid and carbamate formation in NH_3:CO_2 ices - UV irradiation versus thermal processes. Astron. Astrophys. 492 (3), 719–724. http://dx.doi.org/10.1051/0004-6361:200810536.

Bouilloud, M., Fray, N., Bénilan, Y., Cottin, H., Gazeau, M.-C., Jolly, A., 2015. Bibliographic review and new measurements of the infrared band strengths of pure molecules at 25K: H_2O, CO_2, CO, CH_4, NH_3, CH_3OH, HCOOH and H_2CO. Mon. Not. R. Astron. Soc. 451 (2), 2145–2160.

Bramble, M.S., Hand, K.P., 2024. 10 kev electron irradiation of methane ices at ocean world surface temperatures. Icarus 421, 116214.

Brewer, L., Wang, J.L.-F., 1972. Infrared absorption spectra of isotopic ozone isolated in rare-gas matrices. J. Chem. Phys. 56 (2), 759–762. http://dx.doi.org/10.1063/1.1677228, arXiv:https://doi.org/10.1063/1.1677228.

Brown, R.H., Clark, R.N., Buratti, B.J., Cruikshank, D.P., Barnes, J.W., Mastrapa, R.M., Bauer, J., Newman, S., Momary, T., Baines, K., et al., 2006. Composition and physical properties of Enceladus' surface. Science 311 (5766), 1425–1428.

Cassidy, T., Coll, P., Raulin, F., Carlson, R.W., Johnson, R.E., Loeffler, M.J., Hand, K.P., Baragiola, R.A., 2010. Radiolysis and photolysis of icy satellite surfaces: Experiments and theory. Space Sci. Rev. 153 (1–4), 299–315. http://dx.doi.org/10.1007/s11214-009-9625-3.

Cazaux, S., Bossa, J.B., Linnartz, H., Tielens, A.G.G.M., 2015. Pore evolution in interstellar ice analogues. Simulating the effects of temperature increase. Astron. Astrophys. 573, A16. http://dx.doi.org/10.1051/0004-6361/201424466, arXiv:1410.6343.

Chandra, S., Henderson, B.L., Gudipati, M.S., 2025. Radiation sputtering of hydrocarbon ices at Europa-relevant temperatures. arXiv preprint arXiv:2502.00257.

Chen, Y.J., Nuevo, M., Chu, C.C., Fan, Y.G., Yih, T.S., Ip, W.H., Fung, H.S., Wu, C.Y.R., 2011. Photo-desorbed species produced by the UV/EUV irradiation of an H_2O:CO_2:NH_3 ice mixture. Adv. Space Res. 47 (9), 1633–1644. http://dx.doi.org/10.1016/j.asr.2010.12.018.

Chuang, K.J., Jäger, C., Santos, J.C., Henning, T., 2024. Formation of N-bearing complex organic molecules in molecular clouds: Ketenimine, acetonitrile, acetaldimine, and vinylamine via the UV photolysis of C_2H_2 ice. Astron. Astrophys. 687, A7. http://dx.doi.org/10.1051/0004-6361/202348890, arXiv:2405.07855.

Combe, J.-P., McCord, T.B., Matson, D.L., Johnson, T.V., Davies, A.G., Scipioni, F., Tosi, F., 2019. Nature, distribution and origin of CO_2 on Enceladus. Icarus 317, 491–508. http://dx.doi.org/10.1016/j.icarus.2018.08.007.

Congiu, E., Fedoseev, G., Ioppolo, S., Dulieu, F., Chaabouni, H., Baouche, S., Lemaire, J.L., Laffon, C., Parent, P., Lamberts, T., Cuppen, H.M., Linnartz, H., 2012. No ice hydrogenation: A solid pathway to NH_2OH formation in space. Astrophys. J. Lett. 750 (1), L12. http://dx.doi.org/10.1088/2041-8205/750/1/L12.

Cruikshank, D.P., Owen, T.C., Dalle Ore, C., Geballe, T.R., Roush, T.L., De Bergh, C., Sandford, S.A., Poulet, F., Benedix, G.K., Emery, J.P., 2005. A spectroscopic study of the surfaces of Saturn's large satellites: H_2O ice, tholins, and minor constituents. Icarus 175 (1), 268–283.

Cruz-Diaz, G.A., Muñoz Caro, G.M., Chen, Y.J., Yih, T.S., 2014. Vacuum-UV spectroscopy of interstellar ice analogs. II. Absorption cross-sections of nonpolar ice molecules. Astron. Astrophys. 562, A120. http://dx.doi.org/10.1051/0004-6361/201322621, arXiv:1405.7802.

Cuppen, H.M., Linnartz, H., Ioppolo, S., 2024. Laboratory and computational studies of interstellar ices. Annu. Rev. Astron. Astrophys. 62 (1), 243–286. http://dx.doi.org/10.1146/annurev-astro-071221-052732.

Cuppen, H.M., Walsh, C., Lamberts, T., Semenov, D., Garrod, R.T., Penteado, E.M., Ioppolo, S., 2017. Grain surface models and data for astrochemistry. Space Sci. Rev. 212 (1), 1–58.

Demyk, K., Dartois, E., D'Hendecourt, L., Jourdain de Muizon, M., Heras, A.M., Breitfellner, M., 1998. Laboratory identification of the 4.62 μm solid state absorption band in the ISO-sws spectrum of RAFGL 7009s. Astron. Astrophys. 339, 553–560.

Dougherty, M.K., Esposito, L.W., Krimigis, S.M., 2009. Saturn from Cassini–Huygens. http://dx.doi.org/10.1007/978-1-4020-9217-6.

Dougherty, M., Khurana, K., Neubauer, F., Russell, C., Saur, J., Leisner, J., Burton, M., 2006. Identification of a dynamic atmosphere at Enceladus with the Cassini magnetometer. Science 311 (5766), 1406–1409.

Edridge, J.L., Freimann, K., Burke, D.J., Brown, W.A., 2013. Surface science investigations of the role of CO_2 in astrophysical ices. Philos. Trans. R. Soc. A: Math., Phys. Eng. Sci. 371 (1994), 20110578.

Ehrenfreund, P., Boogert, A.C.A., Gerakines, P.A., Tielens, A.G.G.M., van Dishoeck, E.F., 1997. Infrared spectroscopy of interstellar apolar ice analogs. Astron. Astrophys. 328, 649–669.

Ehrenfreund, P., Kerkhof, O., Schutte, W.A., Boogert, A.C.A., Gerakines, P.A., Dartois, E., D'Hendecourt, L., Tielens, A.G.G.M., van Dishoeck, E.F., Whittet, D.C.B., 1999. Laboratory studies of thermally processed H_2O-CH_3OH-CO_2 ice mixtures and their astrophysical implications. Astron. Astrophys. 350, 240–253.

Emery, J., Burr, D., Cruikshank, D., Brown, R., Dalton, J., 2005. Near-infrared (0.8–4.0 μm) spectroscopy of Mimas, Enceladus, Tethys, and Rhea. Astron. Astrophys. 435 (1), 353–362.

Fedoseev, G.S., 2014. Atom addition reactions in interstellar ice-new pathways towards molecular complexity in space. Chem. Phys. 16, 8257.

Fedoseev, G., Chuang, K.-J., van Dishoeck, E.F., Ioppolo, S., Linnartz, H., 2016. Simultaneous hydrogenation and UV-photolysis experiments of NO in CO-rich interstellar ice analogues; linking HNCO, OCN^-, NH_2CHO, and NH_2OH. Mon. Not. R. Astron. Soc. 460 (4), 4297–4309.

Filacchione, G., D'Aversa, E., Capaccioni, F., Clark, R.N., Cruikshank, D.P., Ciarniello, M., Cerroni, P., Bellucci, G., Brown, R.H., Buratti, B.J., Nicholson, P.D., Jaumann, R., McCord, T.B., Sotin, C., Stephan, K., Dalle Ore, C.M., 2016. Saturn's icy satellites investigated by Cassini-VIMS. IV. Daytime temperature maps. Icarus 271, 292–313. http://dx.doi.org/10.1016/j.icarus.2016.02.019, arXiv:1602.02890.

Gao, P., Kopparla, P., Zhang, X., Ingersoll, A.P., 2016. Aggregate particles in the plumes of Enceladus. Icarus 264, 227–238. http://dx.doi.org/10.1016/j.icarus.2015.09.030, arXiv:1506.00713.

Gerakines, P.A., Moore, M.H., Hudson, R.L., 2000. Carbonic acid production in H_2O:CO_2 ices. UV photolysis vs. proton bombardment. Astron. Astrophys. 357, 793–800.

Gerakines, P.A., Schutte, W.A., Ehrenfreund, P., 1996. Ultraviolet processing of interstellar ice analogs. I. Pure ices. Astron. Astrophys. 312, 289–305.

Gerakines, P.A., Schutte, W.A., Greenberg, J.M., van Dishoeck, E.F., 1995. The infrared band strengths of H_2O, CO and CO_2 in laboratory simulations of astrophysical ice mixtures. Astron. Astrophys. 296, 810. http://dx.doi.org/10.48550/arXiv.astro-ph/9409076, arXiv:astro-ph/9409076.

Giuliano, B., Escribano, R., Martín-Doménech, R., Dartois, E., Caro, G.M., 2014. Interstellar ice analogs: Band strengths of H_2O, CO_2, CH_3OH, and NH_3 in the far-infrared region. Astron. Astrophys. 565, A108.

He, J., Emtiaz, S.M., Vidali, G., 2017. Diffusion and clustering of carbon dioxide on non-porous amorphous solid water. Astrophys. J. 837 (1), 65.

Hodyss, R., Johnson, P.V., Orzechowska, G.E., Goguen, J.D., Kanik, I., 2008. Carbon dioxide segregation in 1: 4 and 1: 9 CO_2: H_2o ices. Icarus 194 (2), 836–842.

Hsu, H.-W., Postberg, F., Sekine, Y., Shibuya, T., Kempf, S., Horányi, M., Juhász, A., Altobelli, N., Suzuki, K., Masaki, Y., et al., 2015. Ongoing hydrothermal activities within Enceladus. Nature 519 (7542), 207–210.

Hudgins, D.M., Sandford, S.A., Allamandola, L.J., Tielens, A.G.G.M., 1993. Mid- and far-infrared spectroscopy of ices: Optical constants and integrated absorbances. Astrophys. J. Suppl. 86, 713. http://dx.doi.org/10.1086/191796.

Hudson, R.L., Gerakines, P.A., 2023. Influences on infrared spectra of benzene ices for Titan, comets, and beyond: Annealings, artifacts, and isosbestic points. Planet. Sci. J. 4 (3), 55. http://dx.doi.org/10.3847/PSJ/acc337.

Hudson, R.L., Gerakines, P.A., Yarnall, Y.Y., 2022. Ammonia ices revisited: New IR intensities and optical constants for solid NH_3. Astrophys. J. 925 (2), 156.

Ioppolo, S., Cuppen, H.M., van Dishoeck, E.F., Linnartz, H., 2010. Surface formation of HCOOH at low temperature. Mon. Not. R. Astron. Soc. 410 (2), 1089–1095. http://dx.doi.org/10.1111/j.1365-2966.2010.17515.x, arXiv:https://academic.oup.com/mnras/article-pdf/410/2/1089/3441974/mnras0410-1089.pdf.

Khawaja, N., Postberg, F., Hillier, J., Klenner, F., Kempf, S., Nölle, L., Reviol, R., Zou, Z., Srama, R., 2019. Low-mass nitrogen-, oxygen-bearing, and aromatic compounds in Enceladean ice grains. Mon. Not. R. Astron. Soc. 489 (4), 5231–5243. http://dx.doi.org/10.1093/mnras/stz2280.

Kieffer, S.W., Lu, X., McFarquhar, G., Wohletz, K.H., 2009. A redetermination of the ice/vapor ratio of Enceladus' plumes: Implications for sublimation and the lack of a liquid water reservoir. Icarus 203 (1), 238–241. http://dx.doi.org/10.1016/j.icarus.2009.05.011.

Leto, G., Baratta, G., 2003. Ly-α photon induced amorphization of Ic water ice at 16 kelvin-effects and quantitative comparison with ion irradiation. Astron. Astrophys. 397 (1), 7–13.

Ligterink, N.F.W., Terwisscha van Scheltinga, J., Taquet, V., Jørgensen, J.K., Cazaux, S., van Dishoeck, E.F., Linnartz, H., 2018. The formation of peptide-like molecules on interstellar dust grains. Mon. Not. R. Astron. Soc. 480 (3), 3628–3643. http://dx.doi.org/10.1093/mnras/sty2066, arXiv:1808.00742.

Ligterink, N., Walsh, C., Bhuin, R., Vissapragada, S., van Scheltinga, J.T., Linnartz, H., 2018. Methanol ice co-desorption as a mechanism to explain cold methanol in the gas-phase. Astron. Astrophys. 612, A88.

Linnartz, H., Ioppolo, S., Fedoseev, G., 2015. Atom addition reactions in interstellar ice analogues. Int. Rev. Phys. Chem. 34 (2), 205–237.

Loeffler, M.J., Baragiola, R.A., 2010. Photolysis of solid NH_3 and NH_3-H_2O mixtures at 193 nm. J. Comput. Phys. 133 (21), http://dx.doi.org/10.1063/1.3506577, 214506–214506.

Lv, X.Y., Boduch, P., Ding, J.J., Domaracka, A., Langlinay, T., Palumbo, M.E., Rothard, H., Strazzulla, G., 2014. Thermal and energetic processing of ammonia and carbon dioxide bearing solid mixtures. Phys. Chem. Chem. Phys. (Incorporating Faraday Trans.) 16 (8), 3433–3441. http://dx.doi.org/10.1039/C3CP54027H.

Madey, T.E., Johnson, R.E., Orlando, T.M., 2002. Far-out surface science: radiation-induced surface processes in the solar system. Surf. Sci. 500 (1–3), 838–858.

Magee, B.A., Waite, J.H., 2017. Neutral gas composition of Enceladus' plume - model parameter insights from Cassini-INMS. In: 48th Annual Lunar and Planetary Science Conference. In: Lunar and Planetary Science Conference, p. 2974.

Maity, S., Kaiser, R.I., Jones, B.M., 2015. Formation of complex organic molecules in methanol and methanol-carbon monoxide ices exposed to ionizing radiation - a combined FTIR and reflectron time-of-flight mass spectrometry study. Phys. Chem. Chem. Phys. (Incorporating Faraday Trans.) 17 (5), 3081–3114. http://dx.doi.org/10.1039/C4CP04149F.

Martín-Doménech, R., Manzano-Santamaría, J., Muñoz Caro, G.M., Cruz-Díaz, G.A., Chen, Y.J., Herrero, V.J., Tanarro, I., 2015. UV photoprocessing of CO_2 ice: A complete quantification of photochemistry and photon-induced desorption processes. Astron. Astrophys. 584, A14. http://dx.doi.org/10.1051/0004-6361/201526003, arXiv:1510.05421.

Martins, Z., Price, M.C., Goldman, N., Sephton, M.A., Burchell, M.J., 2013. Shock synthesis of amino acids from impacting cometary and icy planet surface analogues. Nat. Geosci. 6 (12), 1045–1049. http://dx.doi.org/10.1038/ngeo1930.

Mastrapa, R.M., Bernstein, M.P., Sandford, S.A., Roush, T.L., Cruikshank, D.P., Dalle Ore, C.M., 2008. Optical constants of amorphous and crystalline H_2O-ice in the near infrared from 1.1 to 2.6 μm. Icarus 197 (1), 307–320. http://dx.doi.org/10.1016/j.icarus.2008.04.008.

Mastrapa, R., Sandford, S., Roush, T., Cruikshank, D., Dalle Ore, C., 2009. Optical constants of amorphous and crystalline H_2O-ice: 2.5–22 μm (4000–455 cm- 1) optical constants of H_2O-ice. Astrophys. J. 701 (2), 1347.

Matson, D.L., Davies, A.G., Johnson, T.V., Combe, J.-P., McCord, T.B., Radebaugh, J., Singh, S., 2018. Enceladus' near-surface CO_2 gas pockets and surface frost deposits. Icarus 302, 18–26.

Minissale, M., Aikawa, Y., Bergin, E., Bertin, M., Brown, W.A., Cazaux, S., Charnley, S.B., Coutens, A., Cuppen, H.M., Guzman, V., Linnartz, H., McCoustra, M.R.S., Rimola, A., Schrauwen, J.G., Toubin, C., Ugliengo, P., Watanabe, N., Wakelam, V., Dulieu, F., 2022. Thermal desorption of interstellar ices: A review on the controlling parameters and their implications from snowlines to chemical complexity. ACS Earth Space Chem. 6 (3), 597–630. http://dx.doi.org/10.1021/acsearthspacechem.1c00357, arXiv:https://doi.org/10.1021/acsearthspacechem.1c00357.

Minissale, M., Dulieu, F., 2014. Influence of surface coverage on the chemical desorption process. J. Comput. Phys. 141 (1), 014304. http://dx.doi.org/10.1063/1.4885847, arXiv:1406.5594.

Modica, P., Palumbo, M.E., 2010. Formation of methyl formate after cosmic ion irradiation of icy grain mantles. Astron. Astrophys. 519, A22. http://dx.doi.org/10.1051/0004-6361/201014101.

Moore, M.H., Hudson, R.L., 2000. IR detection of H_2O_2 at 80 K in ion-irradiated laboratory ices relevant to Europa. Icarus 145 (1), 282–288. http://dx.doi.org/10.1006/icar.1999.6325.

Muñoz Caro, G., Meierhenrich, U., Schutte, W., Barbier, B., Segovia, A.A., Rosenbauer, H., Thiemann, W.-P., Brack, A., Greenberg, J., 2002. Amino acids from ultraviolet irradiation of interstellar ice analogues. Nature 416 (6879), 403–406.

New, J.S., Kazemi, B., Spathis, V., Price, M.C., Mathies, R.A., Butterworth, A.L., 2021. Quantitative evaluation of the feasibility of sampling the ice plumes at Enceladus for biomarkers of extraterrestrial life. Proc. Natl. Acad. Sci. 118 (37), e2106197118. http://dx.doi.org/10.1073/pnas.2106197118.

Noble, J.A., Theule, P., Mispelaer, F., Duvernay, F., Danger, G., Congiu, E., Dulieu, F., Chiavassa, T., 2012. The desorption of H_2CO from interstellar grains analogues. Astron. Astrophys. 543, A5. http://dx.doi.org/10.1051/0004-6361/201219437.

Noll, K.S., Johnson, R.E., Lane, A.L., Domingue, D.L., Weaver, H.A., 1996. Detection of ozone on Ganymede. Science 273 (5273), 341–343. http://dx.doi.org/10.1126/science.273.5273.341.

Noll, K.S., Roush, T.L., Cruikshank, D.P., Johnson, R.E., Pendleton, Y.J., 1997. Detection of ozone on Saturn's satellites Rhea and Dione. Nature 388, 45–47. http://dx.doi.org/10.1038/40348.

Nölle, L., Postberg, F., Schmidt, J., Klenner, F., Khawaja, N., Hillier, J., Kempf, S., Hsu, S., Srama, R., 2024. Radial compositional profile of Saturn's E-ring indicates substantial space weathering effects. Mon. Not. R. Astron. Soc. 527 (3), 8131–8139. http://dx.doi.org/10.1093/mnras/stad3621.

Öberg, K.I., 2016. Photochemistry and astrochemistry: photochemical pathways to interstellar complex organic molecules. Chem. Rev. 116 (17), 9631–9663. http://dx.doi.org/10.1021/acs.chemrev.5b00694.

Öberg, K.I., Garrod, R.T., van Dishoeck, E.F., Linnartz, H., 2009a. Formation rates of complex organics in UV irradiated CH_3OH-rich ices. I. Experiments. Astron. Astrophys. 504 (3), 891–913. http://dx.doi.org/10.1051/0004-6361/200912559, arXiv:0908.1169.

Öberg, K.I., van Dishoeck, E.F., Linnartz, H., 2009b. Photodesorption of ices I: CO, N_2, and CO_2. Astron. Astrophys. 496 (1), 281–293. http://dx.doi.org/10.1051/0004-6361/200810207, arXiv:0809.1333.

Okabe, H., et al., 1978. Photochemistry of Small Molecules. Vol. 431, Wiley New York.

Porco, C.C., Helfenstein, P., Thomas, P., Ingersoll, A., Wisdom, J., West, R., Neukum, G., Denk, T., Wagner, R., Roatsch, T., et al., 2006. Cassini observes the active south pole of Enceladus. Science 311 (5766), 1393–1401.

Postberg, F., Khawaja, N., Abel, B., Choblet, G., Glein, C.R., Gudipati, M.S., Henderson, B.L., Hsu, H.-W., Kempf, S., Klenner, F., et al., 2018. Macromolecular organic compounds from the depths of Enceladus. Nature 558 (7711), 564–568.

Postberg, F., Sekine, Y., Klenner, F., Glein, C.R., Zou, Z., Abel, B., Furuya, K., Hillier, J.K., Khawaja, N., Kempf, S., et al., 2023. Detection of phosphates originating from Enceladus's ocean. Nature 618 (7965), 489–493.

Potapov, A., Fulvio, D., Krasnokutski, S., Jäger, C., Henning, T., 2022. Formation of complex organic and prebiotic molecules in H_2O: NH_3: CO_2 ices at temperatures relevant to hot cores, protostellar envelopes, and planet-forming disks. J. Phys. Chem. A 126 (10), 1627–1639.

Raunier, S., Chiavassa, T., Marinelli, F., Aycard, J.-P., 2004. Experimental and theoretical study on the spontaneous formation of OCN^- ion: reactivity between HNCO and NH_3/H_2O environment at low temperature. Chem. Phys. 302 (1–3), 259–264.

Schenk, P.M., Clark, R.N., Howett, C.J.A., Verbiscer, A.J., Waite, J.H., 2018. Enceladus and the icy moons of Saturn. http://dx.doi.org/10.2458/azu_uapress_9780816537075.

Schmidt, J.A., Johnson, M.S., Schinke, R., 2013. Carbon dioxide photolysis from 150 to 210 nm: Singlet and triplet channel dynamics, UV-spectrum, and isotope effects. Proc. Natl. Acad. Sci. 110 (44), 17691–17696.

Schutte, W., Allamandola, L., Sandford, S., 1993. An experimental study of the organic molecules produced in cometary and interstellar ice analogs by thermal formaldehyde reactions. Icarus 104 (1), 118–137. http://dx.doi.org/10.1006/icar.1993.1087, URL: https://www.sciencedirect.com/science/article/pii/S0019103583710870.

Schutte, W.A., Boogert, A.C.A., Tielens, A.G.G.M., Whittet, D.C.B., Gerakines, P.A., Chiar, J.E., Ehrenfreund, P., Greenberg, J.M., van Dishoeck, E.F., de Graauw, T., 1999. Weak ice absorption features at 7.24 and 7.41 μm in the spectrum of the obscured young stellar object W 33A. Astron. Astrophys. 343, 966–976.

Sivaraman, B., Jamieson, C.S., Mason, N.J., Kaiser, R.I., 2007. Temperature-dependent formation of ozone in solid oxygen by 5 kev electron irradiation and implications for solar system ices. Astrophys. J. 669 (2), 1414–1421. http://dx.doi.org/10.1086/521216.

Spencer, J.R., Pearl, J.C., Segura, M., Flasar, F.M., Mamoutkine, A., Romani, P., Buratti, B.J., Hendrix, A.R., Spilker, L.J., Lopes, R.M.C., 2006. Cassini encounters Enceladus: Background and the discovery of a south polar hot spot. Science 311 (5766), 1401–1405. http://dx.doi.org/10.1126/science.1121661, arXiv:https://www.science.org/doi/pdf/10.1126/science.1121661. URL: https://www.science.org/doi/abs/10.1126/science.1121661.

Stephan, K., Jaumann, R., Wagner, R., Clark, R.N., Cruikshank, D.P., Giese, B., Hibbitts, C.A., Roatsch, T., Matz, K.-D., Brown, R.H., Filacchione, G., Cappacioni, F., Scholten, F., Buratti, B.J., Hansen, G.B., Nicholson, P.D., Baines, K.H., Nelson, R.M., Matson, D.L., 2012. The Saturnian satellite Rhea as seen by Cassini VIMS. Planet. Space Sci. 61 (1), 142–160. http://dx.doi.org/10.1016/j.pss.2011.07.019.

Stephan, K., Jaumann, R., Wagner, R., Clark, R.N., Cruikshank, D.P., Hibbitts, C.A., Roatsch, T., Hoffmann, H., Brown, R.H., Filacchione, G., Buratti, B.J., Hansen, G.B., McCord, T.B., Nicholson, P.D., Baines, K.H., 2010. Dione's spectral and geological properties. Icarus 206 (2), 631–652. http://dx.doi.org/10.1016/j.icarus.2009.07.036.

Stief, L.J., Payne, W.A., Klemm, R.B., 1975. A flash photolysis-resonance fluorescence study of the formation of $O(^1D)$ in the photolysis of water and the reaction of $O(^1D)$ with H_2, Ar, and He-. J. Comput. Phys. 62 (10), 4000–4008. http://dx.doi.org/10.1063/1.430323.

Tanaka, I., Carrington, T., Broida, H.P., 1961. Photon-dissociation of water: Initial nonequilibrium populations of rotational states of $OH(^2\Sigma^+)$. J. Comput. Phys. 35 (2), 750–751. http://dx.doi.org/10.1063/1.1732000.

Teolis, B., Jones, G.H., Miles, P., Tokar, R., Magee, B., Waite, J., Roussos, E., Young, D., Crary, F., Coates, A.J., et al., 2010. Cassini finds an oxygen–carbon dioxide atmosphere at Saturn's icy moon Rhea. Science 330 (6012), 1813–1815.

Teolis, B.D., Waite, J.H., 2016. Dione and Rhea seasonal exospheres revealed by Cassini CAPS and INMS. Icarus 272, 277–289. http://dx.doi.org/10.1016/j.icarus.2016.02.031.

Terwisscha van Scheltinga, J., 2021. Ice and Gas in Protostellar Clouds and Planet-Forming Disks (Ph.D. thesis). Leiden University.

Terwisscha van Scheltinga, J., Ligterink, N.F.W., Bosman, A.D., Hogerheijde, M.R., Linnartz, H., 2022. The formation of CO_2 through consumption of gas-phase CO on vacuum-UV irradiated water ice. Astron. Astrophys. 666, A35. http://dx.doi.org/10.1051/0004-6361/202142181, arXiv:2208.13789.

van Broekhuizen, F.A., Groot, I.M.N., Fraser, H.J., van Dishoeck, E.F., Schlemmer, S., 2006. Infrared spectroscopy of solid CO-CO_2 mixtures and layers. Astron. Astrophys. 451 (2), 723–731. http://dx.doi.org/10.1051/0004-6361:20052942, arXiv:astro-ph/0511815.

van Broekhuizen, F.A., Keane, J.V., Schutte, W.A., 2004. A quantitative analysis of OCN^- formation in interstellar ice analogs. Astron. Astrophys. 415 (2), 425–436.

van Broekhuizen, F.A., Pontoppidan, K.M., Fraser, H.J., van Dishoeck, E.F., 2005. A 3-5 μm VLT spectroscopic survey of embedded young low mass stars II. Solid OCN^-. Astron. Astrophys. 441 (1), 249–260. http://dx.doi.org/10.1051/0004-6361:20041711, arXiv:astro-ph/0508551.

Waite, J.H., Glein, C.R., Perryman, R.S., Teolis, B.D., Magee, B.A., Miller, G., Grimes, J., Perry, M.E., Miller, K.E., Bouquet, A., et al., 2017. Cassini finds molecular hydrogen in the Enceladus plume: Evidence for hydrothermal processes. Science 356 (6334), 155–159.

Watanabe, N., Kouchi, A., 2002. Efficient formation of formaldehyde and methanol by the addition of hydrogen atoms to CO in H_2O-CO ice at 10 K. Astrophys. J. Lett. 571 (2), L173–L176. http://dx.doi.org/10.1086/341412.

Wolff, A.J., Carlstedt, C., Brown, W.A., 2007. Studies of binary layered CH_3OH/H_2O ices adsorbed on a graphite surface. J. Phys. Chem. C 111 (16), 5990–5999.

Yeo, G., Ford, T., 1990. The infrared spectrum of the hydroxylamine dimer. J. Mol. Struct. 217, 307–323.

Zheng, W., Kaiser, R.I., 2010. Formation of hydroxylamine (NH_2OH) in electron-irradiated ammonia-water ices. J. Phys. Chem. A 114 (16), 5251–5255.